A Measurement of g_2^p and the Longitudinal-Transverse Spin Polarizability

A. Camsonne (Spokesperson),   P. Bosted,   E. Chudakov,
J.-P. Chen (Spokesperson),   J. Gomez,   D. Gaskell,   J.-O. Hansen,
D. Higinbotham,   J. Lerose,   S. Nanda,   A. Saha,   V. Sulkosky
Thomas Jefferson National Accelerator Facility, Newport News VA, 23606

H. Baghdasaryan,   D. Crabb,   D. Day,   R. Lindgren,   N. Liyanage,
B. Norum,   O.A. Rondon,   J. Singh,   K. Slifer[†] (Spokesperson),
C. Smith,   R. Subedi,   S. Tajima,   K. Wang,   X. Zheng
University of Virginia, Charlottesville, VA, Charlottesville, VA 22903

X. Li,   S. Zhou
China Institute of Atomic Energy, Beijing China

T. Averett,   R. J. Feuerbach,   K. Griffioen
The College of William and Mary, Williamsburg, VA 23187

P. Markowitz
Florida International University, Miami, Fl 33199

E. Cisbani,   F. Cusanno,   S. Frullani,   F. Garibaldi
INFN Roma1 gr. coll. Sanita', Rome, Italy

G.M. Urciuoli
INFN Roma1, Rome, Italy

R. De Leo,   L. Lagamba,   S. Marrone
INFN Bari, Bari, Italy

M. Iodice
INFN Roma3, Rome, Italy

W. Korsch
University of Kentucky, Lexington, Kentucky 40506

N. Kochelev

Joint Institute for Nuclear Research, Dubna, Moscow Region, 141980, Russia

M. Mihovilovič,   M. Potokar,   S. Širca

Jožef Stefan Institute and Dept. of Physics, University of Ljubljana, Slovenia

W. Bertozzi,   S. Gilad,
J. Huang,   B. Moffit,   P. Monaghan,
N. Muangma,   A. Puckett,   Y. Qiang,   X.-H. Zhan

Massachusetts Institute of Technology, Cambridge, MA 02139

M. Khandaker,   F. R. Wesselmann

Norfolk State University, Norfolk, VA 23504

K. McCormick

Pacific Northwest National Laboratory, Richland, WA 99352

R. Gilman⋆,   G. Kumbartzki

Rutgers, The State University of New Jersey, Piscataway, NJ 08854
⋆also *Thomas Jefferson National Accelerator Facility, Newport News VA, 23606*

Seonho Choi,   Ho-young Kang,   Hyekoo Kang,
Byungwuek Lee,   Yoomin Oh,   Jeongseog Song

Seoul National University, Seoul 151-747, Korea

G. Ron

Tel Aviv University, Tel Aviv, 69978 Israel

B. Sawatzky

Temple University, Philadelphia PA, 19122

H. Lu,   X. Yan,   Y. Ye,   Y. Jiang

University of Sci. and Tech. of China , Hefei, Anhui, China

and

The Jefferson Lab Hall A Collaboration

Abstract

JLab has been at the forefront of a program to measure the nucleon spin-dependent structure functions over a wide kinematic range, and data of unprecedented quality has been extracted in all three experimental halls. Higher moments of these quantities have proven to be powerful tools to test QCD sum rules and will provide benchmark tests of Lattice QCD and Chiral Perturbation Theory. Precision measurements of $g_{1,2}^n$ and g_1^p have been performed as part of the highly successful 'extended GDH program', but measurements of the g_2^p structure function remain scarce. This is particularly surprising given the intriguing results found in the transverse data. Namely, a three sigma deviation from the Burkhardt-Cottingham sum rule was found at large Q^2 for the proton, while it is satisfied for the neutron at low Q^2. In addition, it was found that NLO χPT calculations are in agreement with data for the generalized polarizability γ_0^n at $Q^2 = 0.1$ GeV^2, but exhibit a significant discrepancy with the longitudinal-transverse polarizability δ_{LT}^n at the same momentum transfer. Clearly, there are serious questions about our understanding of the transverse spin structure function.

24 days of beam in Hall A will allow a measurement of g_2^p in the resonance region. This data will be used to test the Burkhardt-Cottingham sum rule and to extract the fundamental quantities $\delta_{LT}^p(Q^2)$ and $d_2^p(Q^2)$ with high precision. The Q^2 range $0.02 < Q^2 < 0.4$ GeV^2 is chosen to provide unambiguous benchmark tests of χPT calculations on the lower end, while still probing the transition region where parton-like behaviour begins to emerge. This data will also have a significant impact on our theoretical understanding of the hyperfine structure of the proton, and reduce the systematic uncertainty of CLAS experiments which extract the g_1^p structure from purely longitudinal measurements.

---

†Contact person: Karl Slifer, slifer@jlab.org

Foreword

This document is an update to conditionally approved experiment E07-001. It is meant to address the request of PAC31 to strengthen the physics case for the higher Q^2 portion of the run. Specifically, we address three issues raised by the PAC report:

1. Projected results for the BC sum rule and d_2^p are displayed in Figs. 25 and 26 of section 7.2.

2. A discussion of the impact of this data on ongoing calculations of the hyperfine structure of hydrogen is covered in section 4.1.

3. The impact of this data on the systematic error of CLAS experiment EG4 is now discussed in section 4.2.

In addition, we review the relation of the spin polarizability δ_{LT} measured in this experiment to the VCS polarizabilities in section 3.4.1.

<div align="center">Excerpt from PAC31 Report</div>

Measurement and Feasibility: The proposed experiment constitutes a major installation in Hall A requiring significant technical resources. However, none are felt to be insurmountable, and no particular technical obstacles were identified.

Issues: The PAC feels that to justify the resources and time requested, the physics case should be more solidly established. The proposal presently provides little support for the data points at $Q^2 > 0.1$ GeV2 which account for much of the requested beam time, and where XPT calculations (at modest order) may be expected to break down. The PAC finds these kinematic points of importance, but that their value lies elsewhere. One example is the precise BCSR measurements, particularly as SLAC data at higher Q2 suggest a violation of this sum rule. A second important motivation is the systematic-error reduction the proposed data can provide for the generalized GDH measurements at CLAS. This error reduction is mentioned in the proposal, but the influence of g_2 is not quantified. Further, one PAC member pointed out the importance of precise g_2 data on the proton, especially at low Q^2, to ongoing calculations of the hyperfine structure of hydrogen – a physics case which should be explored.

Recommendation: C1=Conditionally Approve w/Technical Review

Contents

1 Introduction

The experimental and theoretical study [1] of the spin structure of the nucleon has provided many exciting results over the years, along with several new challenges. Probes of QCD in the perturbative regime, such as tests of the Bjorken sum rule [2] have afforded a greater understanding of how the spin of the composite nucleon arises from the intrinsic degrees of freedom of the theory. Recently, results have become available from a new generation of JLab experiments that seek to probe the theory in its non-perturbative and transition regimes. Distinct features seen in the nucleon response to the electromagnetic probe indicate that complementary descriptions of the interaction are possible, depending on the resolution of the probe. The low momentum transfer results offer insight into the coherent region, where the collective behavior of the nucleon constituents give rise to the static properties of the nucleon, in contrast to higher Q^2 where quark-gluon correlations are suppressed and parton-like behavior is observed.

There's been a strong commitment at JLab to extract the spin structure functions g_1^n, g_2^n and g_1^p and their moments over a wide kinematic range [3–12]. But at low and moderate Q^2, data on the g_2^p structure function is absent. The lowest momentum transfer that has been investigated is 1.3 GeV^2 by the RSS collaboration [4]. This proposal aims to fill the gap in our knowledge of the proton spin structure by performing a high precision measurement of g_2^p in the range $0.02 < Q^2 < 0.4$ GeV^2. This experiment will address intriguing discrepancies between data and theory for the Burkhardt-Cottingham Sum Rule (see Section 3.2) and the longitudinal-transverse generalized spin polarizability δ_{LT} (see Section 3.4). It will also have significant impact on ongoing calculations of the hyperfine structure of hydrogen (Section 4.1), and substantially reduce one of the leading systematic uncertainties of the EG4 experiment (Section 4.2).

2 Theoretical Background

2.1 The g_2 Structure Function

If we define $q_f(x)dx$ { and $\overline{q}_f(x)dx$ } as the expectation value for the number of quarks { and anti-quarks } of flavor f in the hadron whose momentum fraction lies in the interval $[x, x + dx]$, then in the parton model it can be shown that:

$$F_1(x) = \frac{1}{2} \sum_f z_f^2 \left(q_f(x) + \overline{q}_f(x) \right) \qquad (1)$$

and

$$g_1(x) = \frac{1}{2} \sum_f z_f^2 \left(q_f(x) - \overline{q}_f(x) \right) \tag{2}$$

where the quark charge z_f enters due to the fact that the cross section is proportional to the squared charge of the target. The Callan-Gross [13] relation shows that F_2 can be defined entirely in terms of F_1, but there is no such simple physical interpretation of g_2. This spin-dependent structure function is determined by the x-dependence of the quarks' transverse momenta and the off-shellness, both of which are unknown in the parton model [14].

Ignoring quark mass effect of order $\mathcal{O}(m_q/\Lambda_{QCD})$, g_2 can be separated into leading and higher-twist components as:

$$g_2(x, Q^2) = g_2^{\mathrm{WW}}(x, Q^2) + \overline{g}_2(x, Q^2) \tag{3}$$

where

$$\overline{g}_2(x, Q^2) = - \int_x^1 \frac{\partial}{\partial y} \left[\frac{m_q}{M} \, h_T(y, Q^2) + \zeta(y, Q^2) \right] \frac{dy}{y} \tag{4}$$

To twist-3, there are three contributions to g_2:

1. g_2^{WW} : The leading twist-2 term, which depends only on g_1.

2. h_T : Arises from the quark transverse polarization distribution. Also twist-2, this term is suppressed by the smallness of the quark mass.

3. ζ : The twist-3 part which arises from quark-gluon interactions.

The Wandzura–Wilczek [15] relation:

$$g_2^{\mathrm{WW}}(x, Q^2) = -g_1(x, Q^2) + \int_x^1 \frac{dy}{y} g_1(y, Q^2) \tag{5}$$

describes the leading twist part of the g_2 completely in terms of g_1. In reality, Eq. 5 is a good approximation only in the limit $Q^2 \to \infty$. At typical JLab kinematics, g_2 exhibits strong deviations from leading twist behaviour as discussed in Sec. 3.1. This gives g_2 a unique sensitivity to higher twist, *i.e.* interaction-dependent effects in QCD [14].

2.2 Sum Rules and Moments

Sum rules involving the spin structure of the nucleon offer an important opportunity to study QCD. In recent years the Bjorken sum rule at large Q^2, and the Gerasimov-Drell-Hearn (GDH) sum rule [16] at $Q^2 = 0$, have attracted a concerted experimental and theoretical effort (see for example [17]). Another class of sum rules address the generalized GDH sum [18] and the spin polarizabilities [19]. These sum rules which are based on unsubstracted dispersion relations and the optical theorem relate the moments of the spin structure functions to real or virtual Compton amplitudes, which can be calculated theoretically.

Considering the forward spin-flip doubly-virtual Compton scattering (VVCS) amplitude g_{TT}, and assuming it has an appropriate convergence behavior at high energy, an unsubstracted dispersion relation leads to the following equation for g_{TT} [9, 19]:

$$\text{Re}[g_{TT}(\nu, Q^2) - g_{TT}^{pole}(\nu, Q^2)] = (\frac{\nu}{2\pi^2})\mathcal{P} \int_{\nu_0}^{\infty} \frac{K(\nu', Q^2)\sigma_{TT}(\nu', Q^2)}{\nu'^2 - \nu^2} d\nu', \quad (6)$$

where g_{TT}^{pole} is the nucleon pole (elastic) contribution, $\mathcal{P}$ denotes the principal value integral and K is the virtual photon flux factor. The lower limit of the integration ν_0 is the pion-production threshold on the nucleon. A low-energy expansion gives:

$$\text{Re}[g_{TT}(\nu, Q^2) - g_{TT}^{pole}(\nu, Q^2)] = (\frac{2\alpha}{M^2})I_{TT}(Q^2)\nu + \gamma_0(Q^2)\nu^3 + O(\nu^5). \quad (7)$$

Combining Eqs. (1) and (2), the $O(\nu)$ term yields a sum rule for the generalized GDH integral [17, 18]:

$$
\begin{aligned}
I_{TT}(Q^2) &= \frac{M^2}{4\pi^2\alpha} \int_{\nu_0}^{\infty} \frac{K(\nu, Q^2)}{\nu} \frac{\sigma_{TT}}{\nu} d\nu \\
&= \frac{2M^2}{Q^2} \int_0^{x_0} \Big[g_1(x, Q^2) - \frac{4M^2}{Q^2}x^2 g_2(x, Q^2)\Big] dx. \quad (8)
\end{aligned}
$$

The low-energy theorem relates I(0) to the anomalous magnetic moment of the nucleon, κ, and Eq. (8) becomes the original GDH sum rule [16]:

$$I(0) = \int_{\nu_0}^{\infty} \frac{\sigma_{1/2}(\nu) - \sigma_{3/2}(\nu)}{\nu} d\nu = -\frac{2\pi^2\alpha\kappa^2}{M^2}, \quad (9)$$

where $2\sigma_{TT} \equiv \sigma_{1/2} - \sigma_{3/2}$. The $O(\nu^3)$ term yields a sum rule for the generalized forward spin polarizability [19]:

$$
\begin{aligned}
\gamma_0(Q^2) &= (\frac{1}{2\pi^2}) \int_{\nu_0}^{\infty} \frac{K(\nu, Q^2)}{\nu} \frac{\sigma_{TT}(\nu, Q^2)}{\nu^3} d\nu \\
&= \frac{16\alpha M^2}{Q^6} \int_0^{x_0} x^2 \Big[g_1(x, Q^2) - \frac{4M^2}{Q^2}x^2 g_2(x, Q^2)\Big] dx. \quad (10)
\end{aligned}
$$

8

Considering the longitudinal-transverse interference amplitude g_{LT}, the $O(\nu^2)$ term leads to the generalized longitudinal-transverse polarizability [19]:

$$
\begin{aligned}
\delta_{LT}(Q^2) &= (\frac{1}{2\pi^2})\int_{\nu_0}^{\infty} \frac{K(\nu,Q^2)}{\nu}\frac{\sigma_{LT}(\nu,Q^2)}{Q\nu^2}d\nu \\
&= \frac{16\alpha M^2}{Q^6}\int_0^{x_0} x^2\Big[g_1(x,Q^2)+g_2(x,Q^2)\Big]dx. \quad (11)
\end{aligned}
$$

The Burkhardt-Cottingham Sum Rule

Alternatively, we can consider the covariant spin-dependent VVCS amplitudes S_1 and S_2, which are related to the spin-flip amplitudes g_{TT} and g_{LT}. The unsubtracted dispersion relations for S_2 and νS_2 lead to a super-convergence relation based on Regge asymptotics which is valid for all Q^2:

$$
\int_0^1 g_2(x,Q^2)dx = 0, \quad (12)
$$

where the integration includes the elastic peak. This sum rule was originally proposed by Burkhardt and Cottingham (BC) [20]. At first glance, it appears to be a trivial consequence of the $n = 1$ term of the operator product expansion (OPE) of Γ_2 (See for example [21]). But the expansion is valid only for $n \geq 3$. The OPE actually gives no information about the BC sum rule [14].

The validity of the BC sum rule depends on convergence of the integral, which would fail [22] for example, if g_2 exhibits non-Regge behaviour at low x, or exhibits a delta function singularity at $x = 0$. It is these criteria for a possible violation that have lead some authors to conclude [23] that "the B.C. integral is either zero or infinite".

Higher Moment $d_2(Q^2)$

At large Q^2, the d_2 matrix element is related to the color polarizabilities, which describe how the color electric and magnetic fields respond to the nucleon spin (see for example [35]). At lower momentum transfer, $d_2(Q^2)$ provides a means to study the transition from perturbative to non-perturbative behaviour and to quantify higher twist effects via:

$$
d_2(Q^2) = 3\int_0^1 x^2\Big[g_2(x,Q^2)-g_2^{WW}(x,Q^2)\Big]dx \quad (13)
$$

The lowest twist component in d_2 is twist-3, although higher twists can also contribute at low Q^2. And although d_2 is a higher-twist OPE object, the definition

9

holds for all Q^2. Then d_2 is just the x^2 moment of the difference between g_2 and g_2^{WW} even at low momentum transfer. It must vanish for $Q^2 \to 0$, and $Q^2 \to \infty$ but peaks around 1 GeV^2. In this sense, it represents a measure of QCD complexity. Therefore, it's of crucial importance to map out d_2 over all Q^2.

2.3 Chiral Perturbation Theory

For low energy interactions, it is impractical to deal directly with quarks and gluons in QCD. Instead, processes are best studied in terms of an effective theory that addresses composite hadrons as the degrees of freedom. In the low energy limit, an effective lagrangian can be formed which still reproduces the symmetries and symmetry breaking patterns of the fundamental theory [25]. For this to be a reasonable approach, the eigenvalues of the quark mass matrix have to be small compared to the typical energy scale of any system under consideration.

The central idea of Chiral Perturbation Theory (χPT) is that the massless left and right handed quarks do not interact with each other so that the theory admits a $U(3)_L \times U(3)_R$ symmetry. Explicit breaking of this symmetry is then treated as a perturbation. As with all effective field theories, at some scale the approximation will fail and must be superseded by a more fundamental approach. The applicability range of χPT is an open question, with estimates ranging as high as $Q^2 = 0.2$ GeV^2 [18]. This issue can only be resolved by benchmark measurements of the Q^2 evolution of quantities calculable in χPT.

Chiral perturbation theory calculations are now being used to help Lattice QCD extrapolate to the physical region. One example is the use of the Chiral extrapolation in π mass from a few hundred MeV to the physical mass scale, and from finite to infinite volume. Because of this it is very important to have benchmark tests of the reliability of these calculations to ensure any error does not propagate.

A measurement of δ_{LT} would test χPT by measuring a nucleon observable that is insensitive to contributions from virtual π-Δ intermediate states [46]. These states affect most other nucleon observables, and limit the applicability of χPT for practical purposes. The χPT predictions for δ_{LT} in LO and NLO are parameter-free predictions, the accuracy of which is determined only by the convergence properties of the chiral expansion. A significant disagreement of these ChPT predictions with the measured values of δ_{LT} would indicate substantial short-distance contributions in this observable, and might force theorists to reconsider the relative importance of long-distance (chiral) and short-distance contributions also in other channels, where this issue is overshadowed by the model dependence introduced by the $\pi\Delta$ contributions. Indirectly, these results would impact also on applications of χPT to the study of the quark mass dependence of other observables in lattice QCD simulations ("chiral extrapolation"), where the relative importance of long-

distance and short-distance contributions is often a matter of debate and depends e.g. on the regularization scheme adopted in evaluating the pion loop contributions [46].

3 Existing Data

3.1 The g_2 Structure Function

SLAC experiment E155x [26] represents the most precise DIS measurement of g_2 for the proton and deuteron. The kinematic range was $0.02 \leq x \leq 0.8$ and $0.7 \leq Q^2 \leq 20$ GeV^2. The results (see Fig. 2) are consistent with the leading twist g_2^{WW} prediction, but with large error bars that don't exclude the possibility of higher twist effects. Also in DIS, JLab experiment E97-103 [27] reported a two standard deviation difference from the leading twist expectation for g_2^n. See Fig. 1. The neutron results were extracted from the measured ^{3}He g_2 structure function at $x \approx 0.2$.

The resonance region at lower Q^2 was investigated by the RSS and the E94-010 collaborations at JLab. Fig. 3 shows preliminary proton g_2 data at $Q^2 \approx 1.3$ GeV^2 from RSS [4] compared to g_2^{WW}, the Simula model [28], Hall B model [29] and MAID [17]. Fig. 4 shows ^{3}He g_2 data from E94-010 [3] compared to g_2^{WW}. The constant Q^2 value is indicated in GeV^2 in each panel. While leading twist behaviour gives a reasonable description of the data at large Q^2, it is clearly insufficient to describe the data at low Q^2.
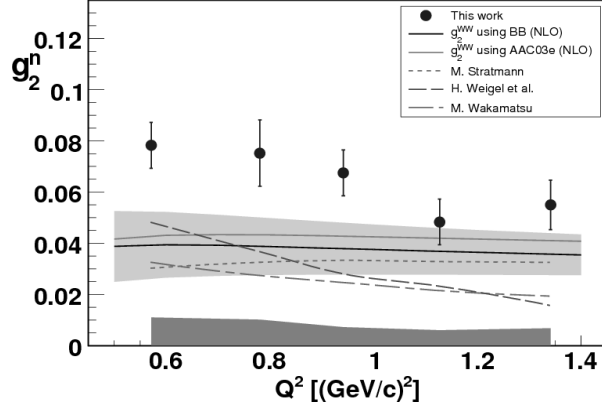
Figure 1: Neutron g_2^n as a function of Q^2 for $x \approx 0.2$. Error bars are statistical. Systematic uncertainties indicated by the lower, dark gray band. The dark solid line, with gray uncertainty band, and the light gray line are calculations of g_2^{WW} using NLO fits to world g_1^n data, evolved to the measured Q^2. *Reproduced from [27].*
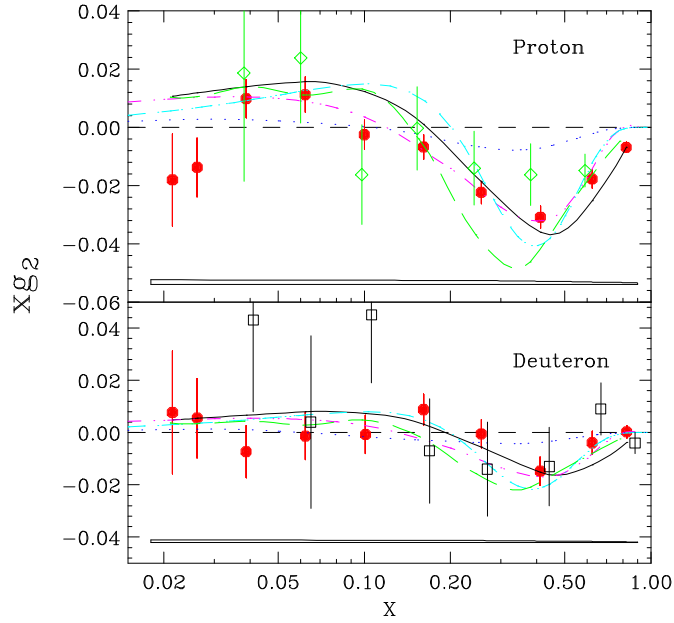
Figure 2: Q^2 averaged (0.8–8.2 GeV^2) xg_2 from E155x (solid circle), E143 (open diamond) and E155 (open square). Error bars are statistical. Also shown is g_2^{WW} (solid line) at the average Q^2 of E155x. Curves are the bag model calculations of Stratmann[30] (dash-dot) and Song[31] (dot) and the chiral soliton models of Weigel and Gamberg[32] (short dash) and Wakamatsu[33] (long dash). *Reproduced from [26].*

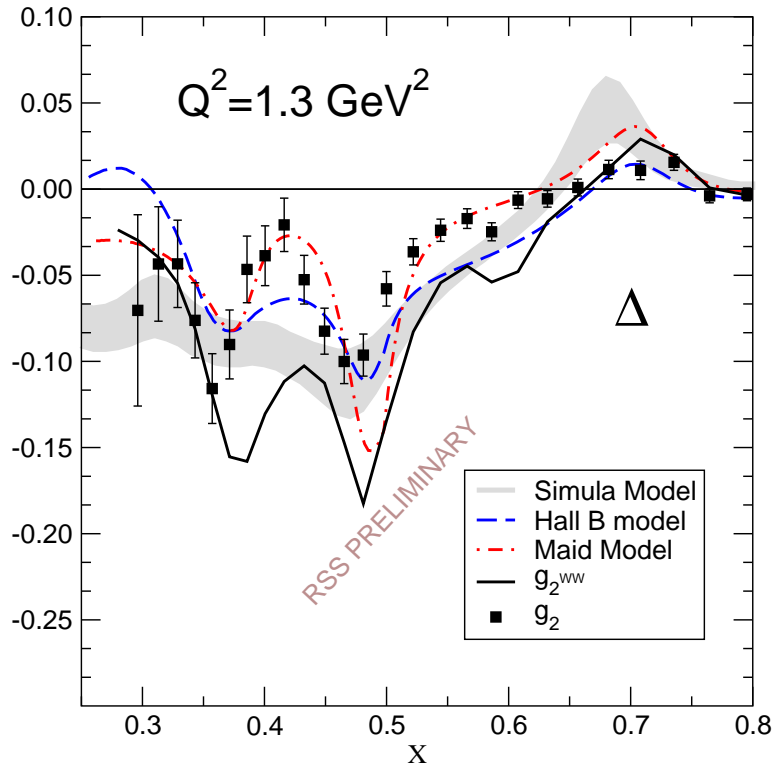Figure 3: Preliminary proton g_2 at $Q^2 \approx 1.3$ GeV^2 from RSS [4] compared to g_2^{WW}, Simula model [28], Hall B model [29] and MAID [17]. Location of the $\Delta(1232)$ resonance indicated at large x.
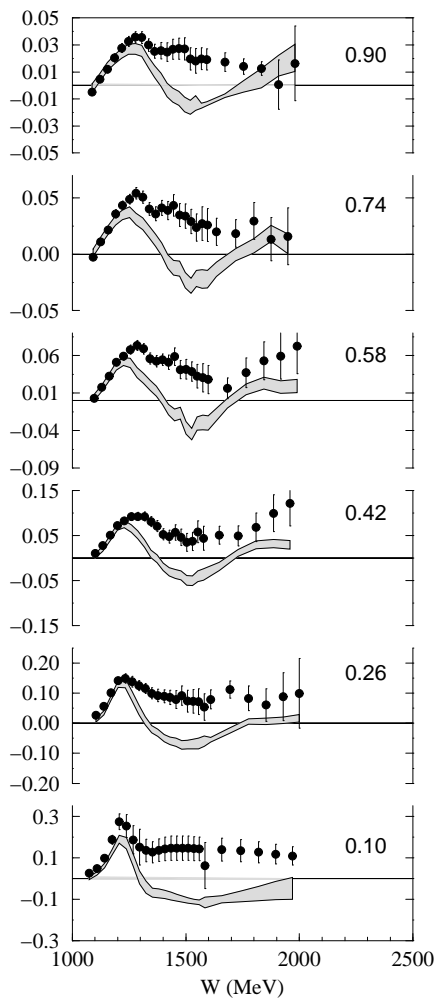
Figure 4: ^{3}He g_2 (filled circle) from E94-010 [3] compared to g_2^{WW} (band). Statistical error only. The constant Q^2 value is indicated in GeV^2 in each panel.

14
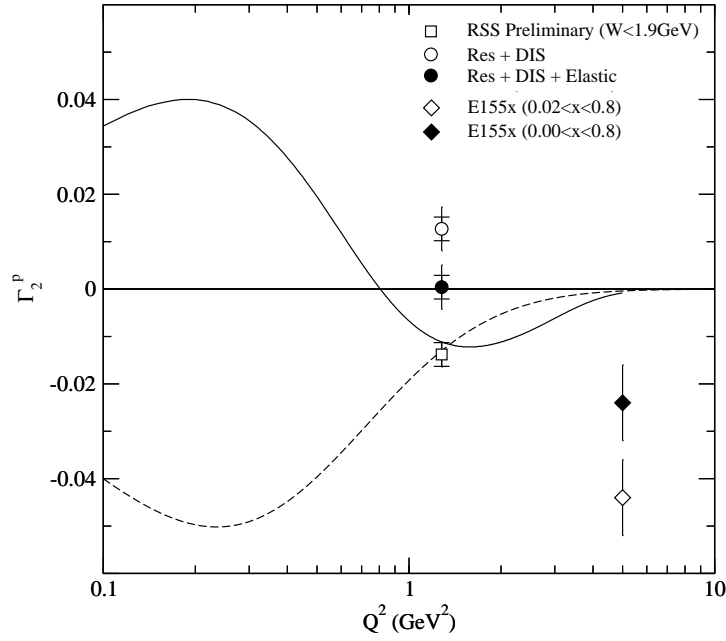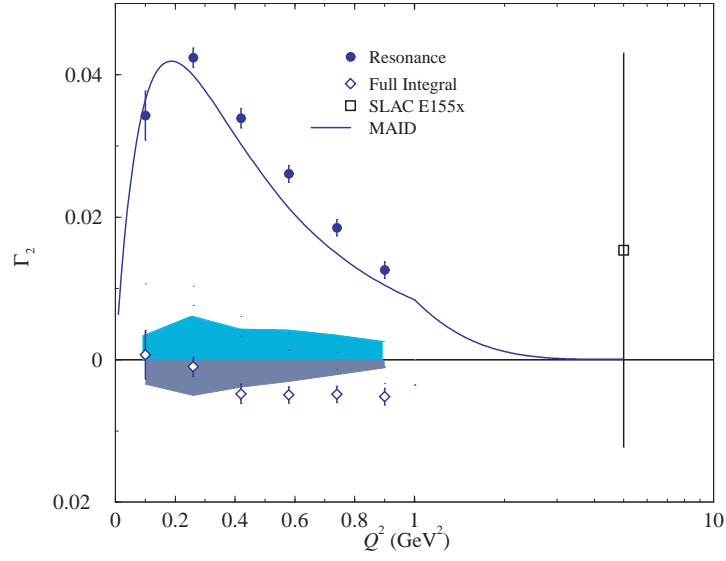
Figure 5: $\Gamma_2(Q^2) = \int g_2 dx$. **Top: Neutron** . E94010 [3] Full circle is the reso-
nance contribution, compared with the MAID model [17]. Open diamonds are the
full $(0 < x < 1)$ integral, including estimates for the elastic and low-x contribu-
tions. Upper, lower bands correspond to the experimental systematic errors, and
the systematic error of the low-x extrapolation, respectively. SLAC E155x [34]
data at $Q^2 = 5$ GeV^2 is also shown. **Bottom: Proton**. Preliminary RSS [4], mea-
sured (open squared). Including estimate of elastic and unmeasured region (filled
circle). E155x [26].

15

3.2 The Burkhardt-Cottingham Sum Rule

Fig. 5 (top panel) shows the Burkhardt-Cottingham integral $\Gamma_2(Q^2) = \int g_2 dx$ for the neutron, which was extracted from Hall A experiment E94-010 [3], from pion threshold to $W = 2$ GeV. The capability to transversely polarize the Hall A ^{3}He target allowed for the precise measurements of g_2 needed for the BC sum. The measured region is shown with solid circles, and the MAID estimate should be compared directly to these resonance region points. The open diamonds represent the full $(0 < x < 1)$ integral, which is evaluated using the well know elastic form factors for the $x = 1$ contribution, and assuming $g_2 = g_2^{WW}$ in the unmeasured low-x region. The upper, lower bands correspond to the experimental systematic errors, and the estimate of the systematic error for the low-x extrapolation, respectively. The total integral exhibits a striking cancellation of the inelastic (resonance+DIS) and elastic contributions, leading to an apparent satisfaction of the Burkhardt-Cottingham sum rule within uncertainties. The SLAC E155x collaboration [34] previously reported a neutron result at high Q^2 (open square), which is consistent with zero but with a rather large error bar.

On the other hand, the SLAC proton result deviated from the BC sum rule prediction by 3 standard deviations [34]. Their result is shown in Fig. 5 (bottom). E155x covered the x-range $0.02 - 0.8$. The extended Q^2 coverage (0.8–8.2 GeV^2) was averaged to 5 GeV^2. For the unmeasured contribution as $x \to 0$, they assumed $g_2 = g_2^{WW}$. Also shown along are the preliminary results from RSS [4] which covered $W < 1.910$ MeV at $Q^2 \approx 1.3$ GeV^2. Open square represents the measured data, while the circular symbols include estimates of the unmeasured region (open) and the elastic contribution at $x = 1$. Inner (outer) error bars represent statistical (total) uncertainty. At this Q^2, the BC sum rule appears to be satisfied within the experimental error.

3.3 Higher Moment $d_2(Q^2)$

Recent neutron d_2 data[‡] is shown in Fig. 6 (top). The experimental results are the open circles, while the grey band represents the systematic uncertainty. The world neutron results from SLAC [34] (open square) and from JLab E99-117 [47] (solid square) are also shown. At low Q^2, the Heavy Baryon (HB) χPT calculation of Kao *et al.* [39] is shown with a dashed line. The Relativisitc Baryon χPT calculation of Bernard *et al.* [38] is very close to the HB curve at this scale, regardless of whether the authors include vector mesons and the Δ contributions. It is not shown on the figure for clarity. The Lattice QCD prediction [49] at $Q^2 = 5$ GeV^2 is negative but

---

[‡]To signify that the entire range $(0 < x < 1)$ is not measured, and the fact Q^2 is finite, the symbol $\bar{d}_2$ is often used.
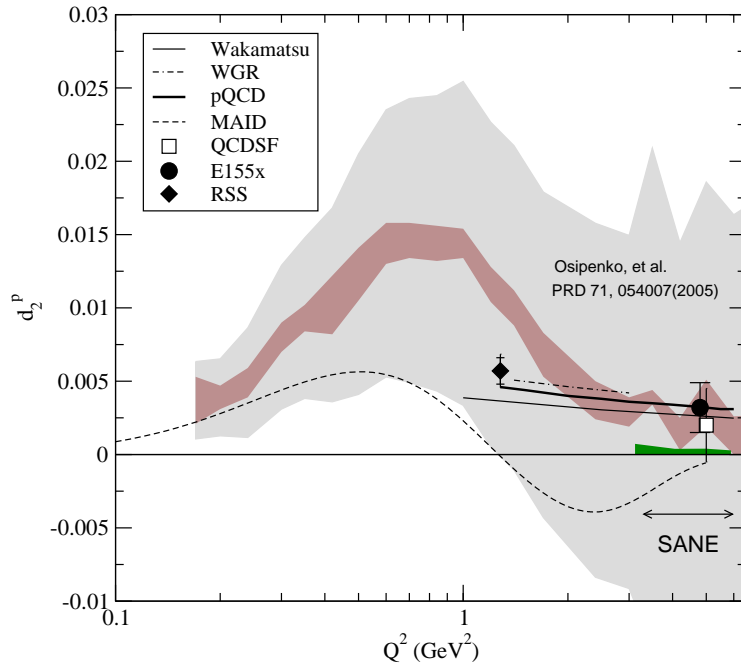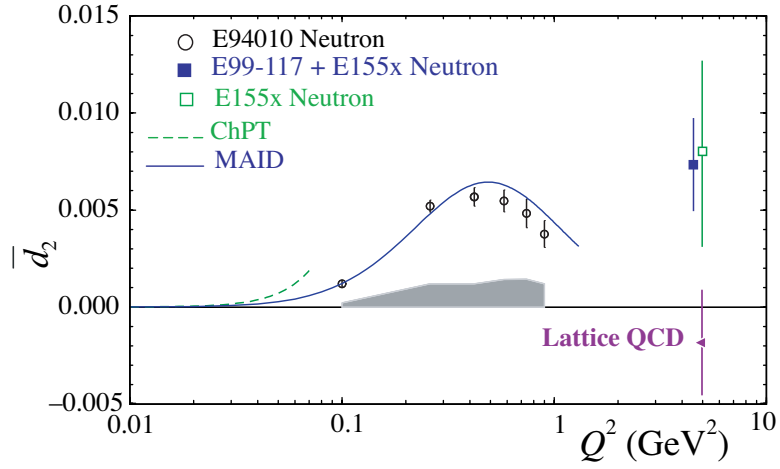
Figure 6: $\bar{d}_2(Q^2)$ **Top: Neutron** Results from JLab [3, 47] and SLAC [34], together with Lattice QCD calculations [49] and the MAID [17] model. **Bottom: Proton** RSS [4], E155x [26], and expected SANE uncertainties [53]. PQCD from [48]. Also shown are a Lattice QCD calculation [49], and the chiral soliton models of WGR [32], and Wakamatsu [33]. The large shaded area is the global analysis from Osipenko et al. [51], with inner (outer) band representing statistical (systematic) uncertainty.

close to zero, and represents a 2σ deviation from the experimental result. We note that all available models (not shown) predict a negative or zero value at large Q^2. As Q^2 increases, the E94010 data reveal a positive, but decreasing $\bar{d}_2^n$.

Fig. 6 (bottom) reveals that the Q^2 evolution of the proton d_2 is not known nearly as well as for the neutron. E155x [26] provides one point at an average Q^2 of 5.0 GeV^2 and RSS [4] measured d_2^p at $Q^2 \approx 1.3$ GeV^2. The large shaded area represents the global analysis of Osipenko et al. [51] using the existing g_1^p data [8] and the MAID [17] model. However, the MAID model disagrees strongly with the existing data, and the authors of [51] note that '*new experimental data on g_2 in the resonance region at different Q^2 values are clearly needed*'.

3.4 Spin Polarizabilities γ_0 and δ_{LT}

The nucleon polarizabilities are fundamental observables that characterize nucleon structure, and are related to integrals of the nucleon excitation spectrum. The electric and magnetic polarizabilities measure the nucleon's response to an external electromagnetic field. Because the polarizabilities can be linked to the forward Compton scattering amplitudes, real photon Compton scattering experiments [40] were performed to measure them. Another polarizability, associated with a spin-flip, is the forward spin polarizability γ_0. It has been measured in an experiment at MAMI (Mainz) [41] with a circularly polarized photon beam on a longitudinally polarized proton target.

The extension of these quantities to the case of virtual photon Compton scattering with finite four-momentum-squared, Q^2, leads to the concept of the generalized polarizabilities. See for example Ref. [42]. Generalized polarizabilities are related to the forward virtual Compton scattering (VCS) amplitudes and the forward doubly-virtual Compton scattering (VVCS) amplitudes [19]. With this additional dependence on Q^2, the generalized polarizabilities provide a powerful tool to probe the nucleon structure covering the whole range from the partonic to the hadronic region. Some generalized polarizabilities data has recently become available for the first time: At MAMI, there is the real photon measurement of γ_0 for the proton [41], and the doubly polarized VCS experiment A1/01-00 [86] has been approved to run. At JLab an extraction of $\gamma_0^n(Q^2)$ and $\delta_{LT}^n(Q^2)$ was performed by E94010 [3], and the EG1b collaboration [8] is finalizing their analysis of data for $\gamma_0^p(Q^2)$.

Since the generalized polarizabilities defined in Eqs. 10 and 11 have an extra $1/\nu^2$ weighting compared to the first moments, these integrals have only a small contribution from the large-ν region and converge quickly, which minimizes the uncertainty due to extrapolation. Measurements of the generalized spin polarizabilities are an important step in understanding the dynamics of QCD in the chiral
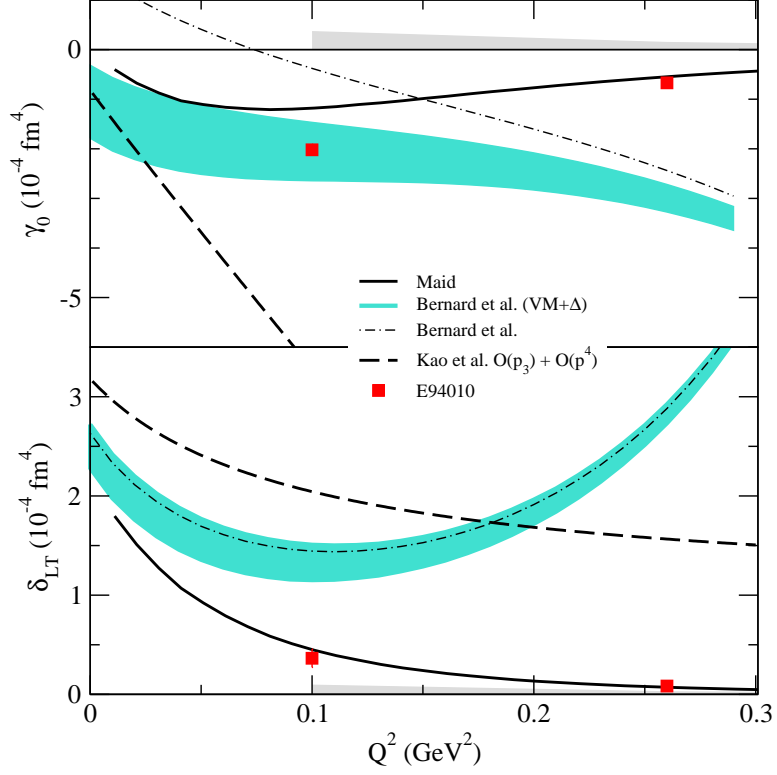
Figure 7: The neutron spin polarizabilities γ_0 (top) and δ_{LT} (bottom). Solid squares represent the results from [3] with statistical uncertainties. The light grey band on the axis represents systematic uncertainties. The heavy dashed curve is the HBχPT calculation of Kao *et al.* [39]. The dot-dashed curve (blue band) is the RBχPT calculation of Bernard *et al.* [38] without (with) the Δ and vector meson contributions. The solid curve is the MAID model [17].

Figure 8: Neutron Forward spin polarizability γ_0 (top panel) and δ_{LT} (bottom panel) with Q^6 weighting. E94010 [3] solid squares are the results with statistical uncertainties. The light bands are the systematic uncertainties. The open squares are the SLAC data [26] and the open diamonds are the Lattice QCD calculations [49].

perturbation region. At low Q^2, the generalized polarizabilities have been evaluated with next-to-leading order χPT calculations [38, 39]. One issue in these calculations is how to properly include the nucleon resonance contributions, especially the Δ resonance. As was pointed out in Refs. [38, 39], while γ_0 is sensitive to resonances, δ_{LT} is insensitive to the Δ resonance.

The first results for the neutron generalized forward spin polarizabilities $\gamma_0(Q^2)$ and $\delta_{LT}(Q^2)$ were obtained at Jefferson Lab Hall A [3]. The results for $\gamma_0^n(Q^2)$ are shown in the top panel of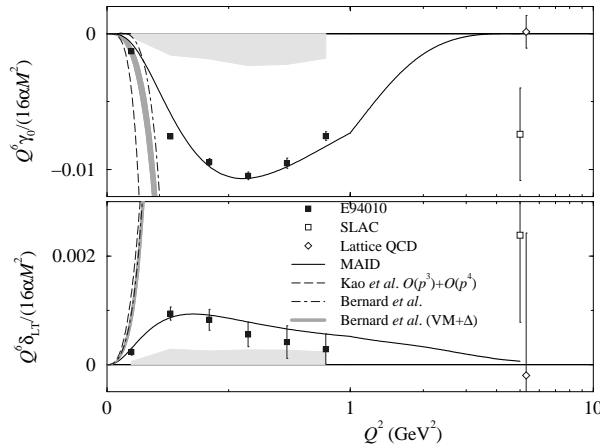 Fig. 7. The statistical uncertainties are smaller than the size of the symbols. The data are compared with a next-to-leading order ($O(p^4)$) HBχPT[§] calculation [39], a next-to-leading order RBχPT[¶] calculation [38], and the same calculation explicitly including both the Δ resonance and vector meson contributions. Predictions from the MAID model [17] are also shown. At the lowest Q^2 point, the RBχPT calculation including the resonance contributions is in good agreement with the experimental result. For the HBχPT calculation without explicit resonance contributions, discrepancies are large even at $Q^2 = 0.1$ GeV^2. This might indicate the significance of the resonance contributions or a problem

---

[§]Heavy Baryon Chiral Perturbation Theory

[¶]Relativistic Baryon Chiral Perturbation Theory

with the heavy baryon approximation at this Q^2. The MAID model reproduces the higher Q^2 data point but underestimates the strength at $Q^2 = 0.1$ GeV^2.

Since δ_{LT} is insensitive to the Δ resonance contribution, it was believed that δ_{LT} should be more suitable than γ_0 to serve as a testing ground for the chiral dynamics of QCD [38, 39]. Fig. 7 shows δ_{LT} compared to χPT calculations and the MAID predictions. While the MAID predictions are in good agreement with the results, it is surprising to see that the data are in significant disagreement with the χPT calculations even at the lowest Q^2, 0.1 GeV^2. This disagreement presents a significant challenge to the present implementation of Chiral Perturbation Theory.

From discussions with theorists, this discrepancy might originate from the short range part of the interaction. Some possible mechanisms which might be responsible are t-channel axial vector meson exchange [44, 45], or an effect of QCD vacuum structure [46]. It is essential to separate different isospins in the t-channel in order to understand the mechanism.

Fig. 8 reveals the Q^2 evolution of the neutron spin polarizabilities. It is expected that at large Q^2, the Q^6-weighted spin polarizabilities become independent of Q^2 (scaling) [19]. No evidence for scaling is observed in the neutron data. It is interesting to note that the deep-inelastic-scattering (DIS) Wandzura-Wilczek relation [15] leads to a relation between γ_0 and δ_{LT}:

$$\delta_{LT}(Q^2) \to \frac{1}{3}\gamma_0(Q^2) \quad \text{as} \quad Q^2 \to \infty. \tag{14}$$

which implies a sign change of one of the polarizabilities at finite Q^2.

3.4.1 Relation of δ_{LT} to the VCS polarizabilities

Generalized Polarizabilities [42] are fundamental observables that characterize the nucleon properties. There are a number of independent Generalized Spin Polarizabilities. VCS experiments, especially doubly polarized VCS experiment, such as A1/01-00 [86] which was approved to run for 300 hours at MAINZ, access some combination of these observables. The expected sensitivity of these measurements is shown in Fig. 9 for 2000 hours.

The Forward Generalized Spin Polarizabilities, γ_0 and δ_{LT}, can be accessed with polarized inclusive electron scattering via the sum rules. The forward longitudinal-longitudinal spin polarizability, γ_0, is closely related to the VCS accessible generalized spin polarizabilities. In the limit $Q^2 = 0$:

$$\gamma_0 = \gamma_1 - \gamma_3 - 2\gamma_4 \tag{15}$$

where γ_i, $(i = 1 \ldots 4)$ are the generalized spin polarizabilities. The unique combination γ_0 measures is not accessible with VCS experiments, and therefore measurements of γ_0 are complementary to the VCS experiments.
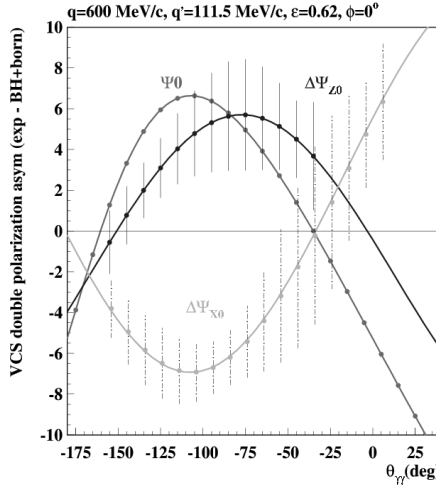
Figure 9: Angular evolutions of the 3 relevant quantities obtained in an in-plane measurement at Mainz, Ψ_0, $\Delta\Psi_0(h,z)$ and $\Delta\Psi_0(h,x)$. The investigated angular range with the accuracy obtained in 2000 hours at $q' = 111.5$ MeV/c would allow to extract the individual GPs. *Reproduced from Ref. [86].*

The longitudinal-transverse spin polarizability δ_{LT} to be measured in this proposal (E07-001), is very special and does not have a simple relation to the other VCS generalized spin polarizabilities. Since it is the L-T interference, it exhibits unique sensitivity. For example, it has very little contribution from the N-to-Δ transition, and allows us to access some physics aspects which would otherwise be masked. In addition, it is much easier to measure and with much higher precision than the doubly polarized VCS experiments as demonstrated in Fig. 9.

Sect 3.3 of Ref. [87] further discusses the relationship between the VVCS spin polarizabilities γ_0 and δ_{LT}, and the VCS polarizabilities. We quote directly below:

> It must be emphasized that the Generalized Polarizabilities [*ed: γ_0 and δ_{LT}*] are not the same as the ones introduced in the previous sections. In VCS we have only one virtual photon, whereas in VVCS ... we have two virtual photons, with identical virtuality. These two types of polarizabilities are however connected in the limit $Q^2 \to 0$.

3.5 The g_1^p Structure Function

The g_1^p structure function has been measured with high precision in the resonance region over a wide range of Q^2 [4, 8, 11]. Due to space constraints we will not discuss this data in detail other than to give an indication of the data quality in Fig. 10,
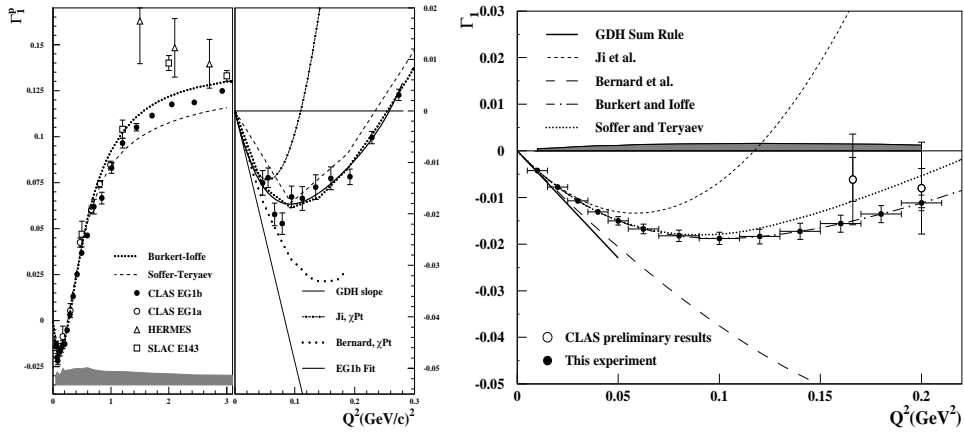
Figure 10: **Left:** Preliminary proton $\Gamma_1(Q^2)$ from EG1b [8], together with published results from EG1a [5], SLAC [34] and HERMES [37]. Model predictions from the Soffer-Teryaev [54] and Burkert-Ioffe [55]. The insets show comparisons with the NLO χPT predictions by Ji *et al.* [56], and Bernard *et al.* [38]. **Right:** Projected proton $\Gamma_1(Q^2)$ for EG4 at low Q^2. *Reproduced from [11].*

which displays the preliminary proton results for $\bar{\Gamma}_1(Q^2)$ from the EG1b [8] experiment, together with the published results from EG1a [5, 6], SLAC [34] and HERMES [37]. The error bar indicates the statistical uncertainty while the band on the axis represents the systematic uncertainty. At $Q^2 = 0$, the slope of Γ_1 is predicted by the GDH sum rule. χPT calculations by Ji *et al.* [56] using HBχPT, and by Bernard *et al.* [38] with and without the inclusion of vector mesons and Δ degrees of freedom are also shown. The calculations are in reasonable agreement with the data in the range $0.05 < Q^2 < 0.1$ GeV^2. The χPT calculations start to show disagreement with the data above $Q^2 \approx 0.06$ GeV^2. At moderate and large Q^2, the data are compared with two model calculations [54, 55], both of which reproduce the data reasonably well.

At the low Q^2 relevent to this proposal g_1^p has been measured with high precision by the EG4 [11] collaboration and the projected results are also shown in Fig. 10 (right panel). For further discussion of the state of measurements of g_1^p, we refer the interested reader to the reviews in Refs. [9, 51] and the experiments [4, 8, 43].

3.6 Ongoing Analyses

Several recent spin structure experiments are in the process of analyzing existing data. These results should be available soon. For example, an extraction of γ_0^p will be performed from the EG1b longitudinal asymmetry data [8] down to $Q^2 \approx 0.05$ GeV^2. The preliminary results [5] show a large deviation from the χPT calculations of Refs. [38, 39]. Neutron(^{3}He) longitudinal and transverse data [10] has also been taken at Q^2 down to 0.02 GeV^2. A longitudinal measurement aimed at extracting g_1 for the proton and deuteron [11] reached similar Q^2. Preliminary results [4] for the proton d_2 and BC integral at $Q^2 \approx 1.3$, will also soon be available.

3.7 Experimental Status Summary

In summary, a large body of nucleon spin-dependent cross-section and asymmetry data has been collected at low to moderate Q^2 in the resonance region. These data have been used to evaluate the Q^2 evolution of moments of the nucleon spin structure functions g_1 and g_2, including the GDH integral, the Bjorken sum, the BC sum and the spin polarizabilities. The BC sum rule for the neutron is observed to be satisfied within uncertainties due to a cancellation between the inelastic and elastic contributions. The situation for the proton is less clear, with a three sigma violation found at $Q^2 = 5$ GeV^2, and preliminary data from [4] in final analysis at $Q^2 \approx 1.3$ GeV^2.

At low Q^2, available next-to-leading order χPT calculations have been tested against data and found to be in reasonable agreement for $0.05 < Q^2 < 0.1$ GeV^2 for the GDH integral $I(Q^2)$, $\Gamma_1(Q^2)$ and the forward spin polarizability $\gamma_0(Q^2)$. Although it was expected that the χPT calculation of δ_{LT} would offer a faster convergence because of the absence of the Δ contribution, the experimental data show otherwise. None of the available calculations can reproduce δ_{LT} at Q^2 of 0.1 GeV^2. This discrepancy presents a significant challenge to our theoretical understanding of χPT. To better understand the δ_{LT} puzzle, or more importantly, to better understand what the puzzle means in terms of the Chiral dynamics, we need both theoretical and experimental efforts. A natural question is whether this discrepancy also exists in the proton case. Testing the isospin dependence would help shed light on the problem. It is of great interest to have a measurement of δ_{LT}^p in the low Q^2 region where the Chiral Perturbation Theory calculations are expected to work.

Overall, we find the case that the neutron spin structure functions g_1^n and g_2^n have been measured to a high degree of precision. This has stimulated an intense amount of theoretical work and has led to many interesting insights. The case is equally impressive for the g_1^p structure function, where high quality data exists

over a wide range in Q^2. However, data is lacking for g_2^p for $Q^2 < 1.3$ GeV^2. For a complete understanding of the nucleon spin structure, g_2^p data in this region is needed.

4 Additional Motivations

4.1 Calculations of the Proton Hyperfine Structure

As recently discussed by Nazaryan, Carlson and Griffioen(NCG) [77], the hyperfine splitting in the hydrogen ground state has been measured to a relative accuracy of 10^{-13}:

$$\Delta E = 1420.405\ 751\ 766\ 7(9)\ \text{MHz}$$

but calculations of this fundamental quantity are only accurate to a few parts per million. The splitting is conventionally expressed in terms of the Fermi energy E_F as $\Delta E = (1 + \delta)E_F$ where the correction δ is given by:

$$\delta = 1 + (\delta_{\text{QED}} + \delta_R + \delta_{small}) + \Delta_S \tag{16}$$

Here, Δ_S is the proton structure correction and has the largest uncertainty. The δ_R term accounts for recoil effects, and δ_{QED} represents the QED radiative correction, which is known to very high accuracy. We've collected the hadronic and muonic vacuum polarizations and the weak interaction correction into δ_{small}. Numerical values for all these quantities are given in Table 1.

Δ_S depends on ground state and excited properties of the proton. It is conventionally split into two terms:

$$\Delta_S = \Delta_Z + \Delta_{\text{pol}} \tag{17}$$

where the first term can be determined from elastic scattering[†]:

$$\Delta_Z = -2\alpha m_e r_Z \left(1 + \delta_Z^{\text{rad}}\right) \tag{18}$$

The Zemach [79] radius r_Z depends on the electric and magnetic form factors of the proton, and is given by:

$$r_Z = -\frac{4}{\pi} \int_0^\infty \frac{dQ}{Q^2} \left[G_E(Q^2) \frac{G_M(Q^2)}{1 + \kappa_p} - 1 \right] \tag{19}$$

where δ_Z^{rad} is the radiative correction.

E_F [MHz]	1 418.840 08	$\pm$	0.000 02
δ_{QED}	0.001 056 21	$\pm$	0.000 000 001
δ_R	0.000 005 84	$\pm$	0.000 000 15
$\delta_{\mu\mathrm{vp}}$	0.000 000 07	$\pm$	0.000 000 02
δ_{hvp}	0.000 000 01		
δ_{weak}	0.000 000 06		

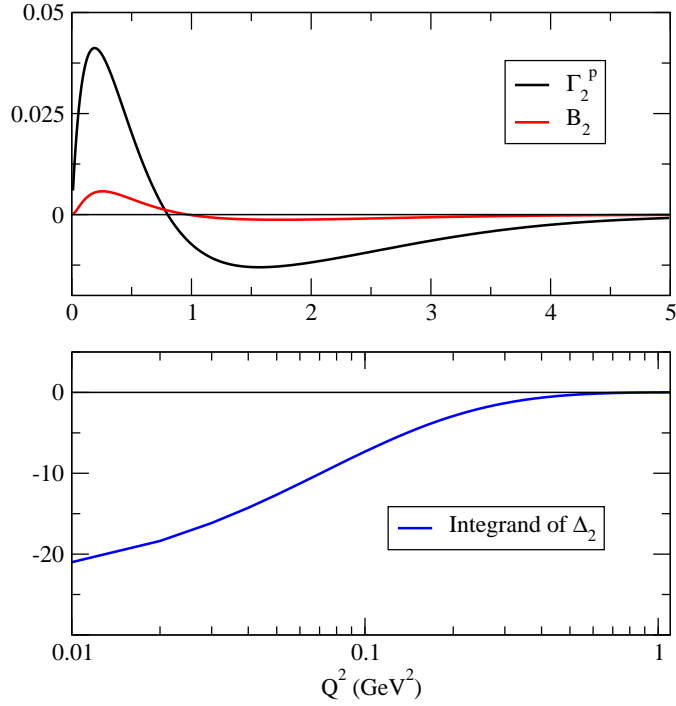Table 1: Numerical values from [77] and [85] and references therein.

Figure 11: MAID [17] model prediction for Γ_2, B_2 and the integrand of Δ_2. Top panel horizontal axis is linear while bottom panel is logarithmic.

The second term, Δ_{pol}, which is of interest to this proposal, involves contributions where the proton is excited. See Refs. [80–84].

$$\Delta_{\mathrm{pol}} = \frac{\alpha m_e}{\pi g_p m_p}(\Delta_1 + \Delta_2), \tag{20}$$

Δ_1 involves the Pauli form factor and the g_1 structure function, while Δ_2 depends only on the g_2 structure function:

$$\Delta_2 = -24m_p^2 \int_0^\infty \frac{dQ^2}{Q^4} B_2(Q^2). \tag{21}$$

where

$$B_2(Q^2) = \int_0^{x_{\mathrm{th}}} dx\, \beta_2(\tau) g_2(x, Q^2), \tag{22}$$

and

$$\beta_2(\tau) \;\; = \;\; 1 + 2\tau - 2\sqrt{\tau(\tau+1)}, \tag{23}$$

Here $\tau = \nu^2/Q^2$, and x_{th} represents the pion production threshold.

NCG [77] utilized the latest data available [5], to determine Δ_1. But to evaluate Δ_2 they were forced to rely heavily on models since there is little g_2 data for the proton: E155 measured g_2^p at large Q^2 [26], and the RSS collaboration [4] pushed down to 1.3 GeV^2 but otherwise the data is lacking. This is significant since the Q^2 weighting of Eq. 21 emphasizes the low momentum transfer region as demonstrated in Fig. 11.

Figs. 1 to 4 showed comparisons of g_2 data to g_2^{WW} and to several models, and revealed that while leading twist behaviour gives a reasonable description of the data at large Q^2, it is clearly insufficient to describe the data at low Q^2. The inherent uncertainty in the models is reflected in the predictions for $|\Delta_2/\Delta_1|$ presented in NCG [77]. The CLAS model predicts a 9% contribution to Δ_{pol}, while in the Simula model it is 52%. Neither model is strongly favored when compared to the existing data as shown in Fig. 3. Precision data at low Q^2 is needed to clarify this situation. Fig. 11 reveals that Δ_2 is dominated by the contribution below 0.4 GeV^2 where this experiment will measure g_2^p.

For this proposal, we evaluated $\Delta_2 = -1.98$ from the MAID model**, while the CLAS model [29] and the Simula model predict $\Delta_2 = -0.57 \pm 0.57$, and

---

† See the update to JLab proposal PR-07-004 [78] for discussion of Zemach radius determination.
** Integrated over the region $W \leq 2$ GeV and $Q^2 \leq 5$ GeV^2.

-1.86 ± 0.37 respectively. NCG [77] utilized the CLAS model with 100% assumed uncertainty on g_2 to obtain:

$$\Delta_{pol} = (1.3 \pm 0.3) \text{ ppm}$$

The total uncertainty projected for this experiment is better than 10%, so we can expect the published error on Δ_2 to improve by an order of magnitude from ±0.57 to ±0.06, and the error contribution of g_2 to Δ_{pol} to decrease from 0.13 ppm to 0.013 ppm. However, we note that the disparity among model predictions is large, which is natural considering the lack of data in this region. For this reason, 100% uncertainty may have been optimistic for the unmeasured quantity g_2^p.

4.2 Impact on EG4 Extraction of g_1^p

The Hall B EG4 [11] experiment ran in 2006, and will extract g_1^p at low Q^2 from a longitudinally polarized cross section measurement. The systematic uncertainty arising from the unmeasured transverse contribution to g_1 is detailed along with the full error budget of EG4 in Table 2.

The EG4 uncertainty arising from the unknown g_2 was estimated in Ref. [11] by noting that the longitudinal polarized cross section $\Delta\sigma_\parallel$ depends on g_2 as follows:

$$\Delta\sigma_\parallel \quad \propto \quad \left(E + E'\cos\theta\right)g_1 - 2Mxg_2 \tag{24}$$

Then, the kinematically weighted contribution of g_2

$$\frac{c_2}{c_1} = \frac{2Mxg_2}{\left(E + E'\cos\theta\right)g_1} \tag{25}$$

was evaluated[††] from a model [29] and is shown in Fig. 12. The g_2 contribution is small for the lowest Q^2, but increases with the momentum transfer and is a leading uncertainty at large Q^2. Assuming the 7-9% projected error of this experiment (detailed in Table 4), EG4 can expect a reduction of the systematic due to g_2 to less than 1 percent for all Q^2.

[††]We note that although models can give an estimate of the g_2 contribution, the difference between available models in this region is large and the the only way to actually quantify the transverse contribution is to experimentally measure g_2 or the transversely polarized cross section.

EG4 Systematic Uncertainty	Value(%)
Beam charge asymmetry	-
Beam and target polarization	1-2
^{15}N background	1-2
Luminosity and filling factor	3.0
Electron efficiency	≤ 5
Radiative Corrections	5.0
Modeling of g_2	1-10†
Extrapolation $(x \rightarrow 0)$	1-10†

Table 2: Summary of systematic errors on the generalized GDH integral for EG4 experiment. Values are from Ref. [11]. Dagger $\dagger$ indicates that value is Q^2-dependent.
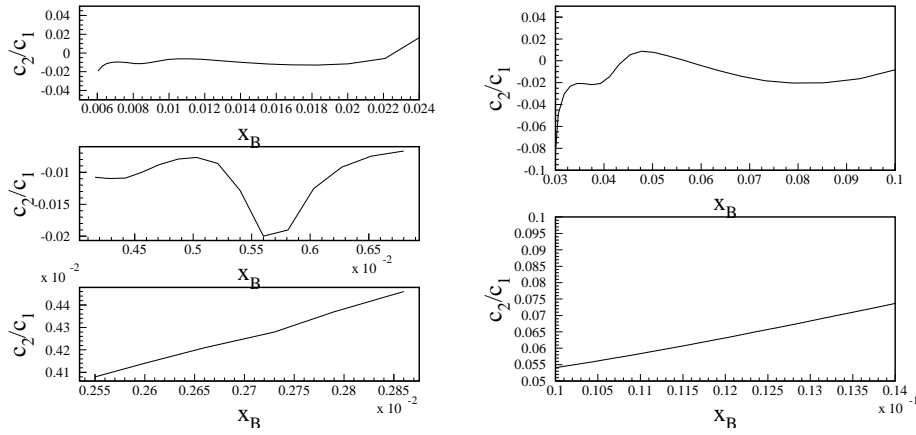

Figure 12: Ratio between the g_2 and g_1 term of the spin dependent cross section for $Q^2 = 0.01$ GeV^2 (left) and beam energy of 1.1, 1.6, and 2.4 GeV (top to bottom), and for $Q^2 = 0.05$ GeV^2 (right) and beam energy of 2.4 GeV and 3.2 GeV (top to bottom). *Reproduced from [11].*
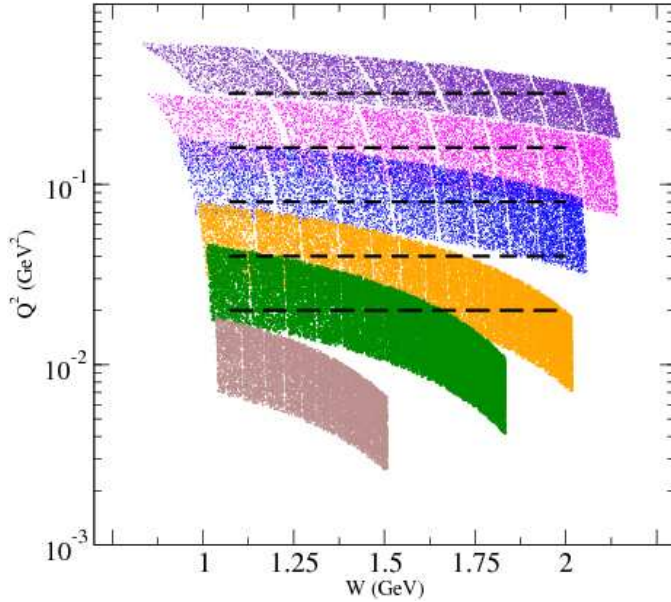
Figure 13: Kinematic coverage. Specific beam energies and angles are detailed in Table 6. Dashed lines represent the interpolation to constant Q^2.

5 Proposed Experiment

We plan to perform an inclusive measurement at forward angle of the proton spin-dependent cross sections in order to determine the g_2^p structure function in the resonance region for $0.02 < Q^2 < 0.4$ GeV^2. The kinematic coverage, shown in Fig. 13, complements experiment EG4 [11]. Data will be measured in the transverse configuration for all energies. In addition, beamtime will be dedicated to the longitudinal configuration for one energy, in order to provide some overlap and cross check of the EG4 data. Kinematic details are listed in Table 6.

This experiment will require the baseline Hall A equipment, with the addition of the septa magnets, and the JLab/UVa polarized target. Adapting the polarized target to Hall A will require extensive technical support from JLab. In particular, we will request:

1. Installation of the UVA/JLab 5 T polarized target.

2. Installation of an upstream chicane and associated support structures.

3. Installation of the slow raster, and the Basel Secondary Emission Monitor (SEM).

30

4. Installation of a local beam dump.

5. Operation of the beamline instrumentation for 50-100 nA beam.

We examine these requirements in detail in the following sections.

5.1 Polarized Target

The polarized target has been successfully used in experiments E143/E155/E155x at SLAC and E93-026 and E01-006 at JLab. This target operates on the principle of Dynamic Nuclear Polarization, to enhance the low temperature (1 K), high magnetic field (5 T) polarization of solid materials (ammonia, lithium hydrides) by microwave pumping. The polarized target assembly contains several target cells of variable length (0.5-3.0 cm) that can be selected individually by remote control to be located in the uniform field region of a superconducting Helmholtz pair. The permeable target cells are immersed in a vessel filled with liquid Helium and maintained at 1 K by use of a high power evaporation refrigerator.

The target material is exposed to 140 GHz microwaves to drive the hyperfine transition which aligns the nucleon spins. The DNP technique produces proton polarizations of up to 90% in the NH_3 target. The heating of the target by the beam causes a drop of a few percent in the polarization, and the polarization slowly decreases with time due to radiation damage. Most of the radiation damage can be repaired by annealing the target at about 80 K, until the accumulated dose reached is greater than about 17×10^{15} e$^-$/cm^2, at which time the target material needs to be replaced. The luminosity of the polarized material in the uniform field region is approximately 85×10^{33} cm^{-2} Hz.

5.2 Chicane

To access g_2^p, the polarization direction will be held perpendicular to the beam axis for the majority of the experiment. This will create a non-negligible deflection of low energy electrons, so to ensure proper transport of the beam, a chicane will be employed. The design, (courtesy of J. Benesch [74]), utilizes the existing Hall C HKS magnets and is shown in Fig. 14. The first dipole will be located 10 meters upstream of the target and gives the beam a kick out of the horizontal plane. The second dipole, which is 4 meters upstream, is mounted on a hydraulic support with a vertical range of 85 cm, and is used to bend the beam back on the target with the required angle to compensate for the 5 Tesla field. Beam Position Monitors (BPMs) will be placed along the chicane line before and after each magnet to ensure proper transport of the beam. Table 3 lists the deflection angles that will be created by the 5 T target field for each incident energy.
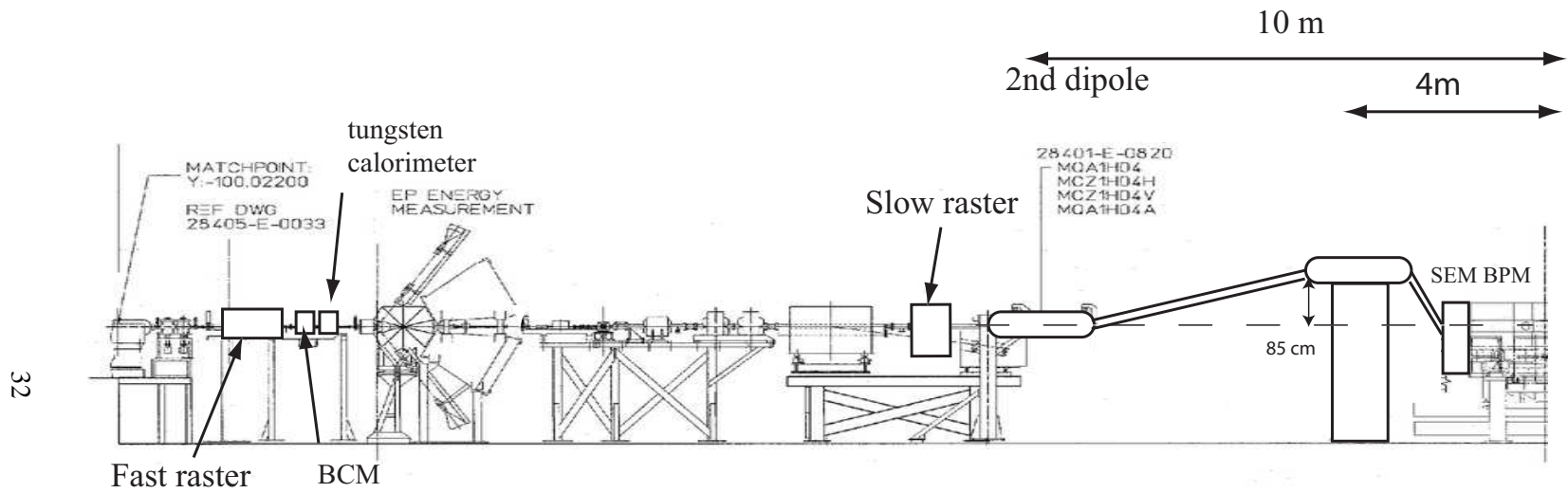
Figure 14: Beamline schematic indicating the location of the fast/slow rasters, Secondary Emission Monitor (SEM), tungsten calorimeter and the chicane magnets. The second dipole is located on a hydraulic stand in order to accommodate the range of vertical displacements needed (see Table 3). Distances are with respect to the polarized target center, at the far right of the diagram.

Energy	Deflection Angle
(GeV)	(deg)
1.1	11.7
1.7	7.6
2.2	5.9
3.3	3.9
4.4	2.9

Table 3: Vertical deflection of the incident electron beam due to the 5 T target field.

5.3 Raster

The existing Hall A fast raster will be used to generate a pattern up to 4 mm x 4 mm and will remain in its standard location (see Fig. 14). The slow raster will be located just upstream of the target, and can increase the final size up to 2.5 cm x 2.5 cm, although we will use a smaller spotsize. A 2 inch wide beam pipe will be used starting after the slow raster.

5.4 Secondary Emission Monitor

To ensure proper reconstruction of target variables given the large raster size, we will utilize the Basel Secondary Emission Monitor (SEM)[‡‡]. This device was used under similar conditions in Hall C and provided an accuracy of better than 1 mm for currents as low as 10 nA. It is insensitive to the target magnetic field.

5.5 Exit beam pipe and beam dump

The low currents employed in this experiment allow for the use of a local beam dump just downstream of the target. The connection from the vacuum chamber to the exit beam pipe will need to be modified to accommodate the vertical deflection of the beam, and the coupling to the beam pipe going to the beam dump. We plan to move the target position upstream by 25 cm, in order to produce a two inch gap between the two septa at six degrees. A two inch beam pipe is sufficient to accommodate the rastered beam and expected multiple scattering.

A helium bag will be used to transport the beam past the septa. This allows for different exit angles. Connection to the usual beam pipe will be made at 5 meters downstream, in order to allow for 'straight-thru' passage of the beam to the standard beam dump when necessary: for example during Moller measurements

---

[‡‡]Also referred to as SEE for **s**econdary **e**lectron **e**mission.
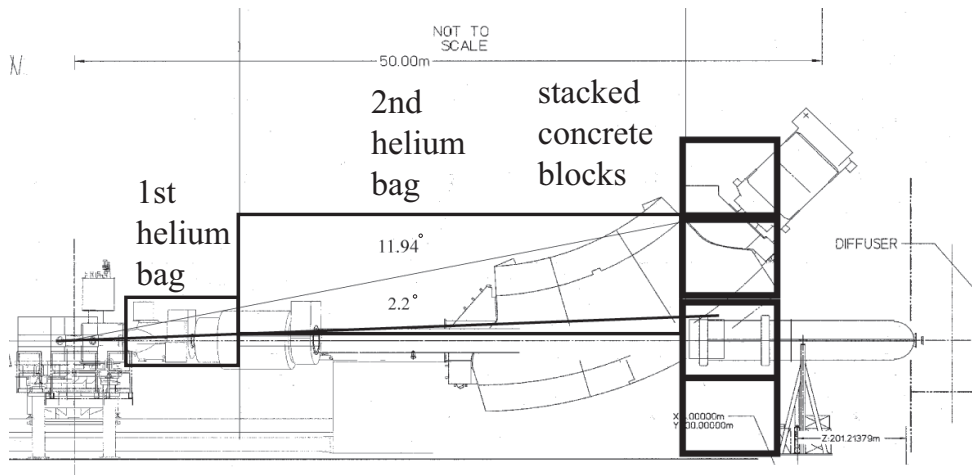
Figure 15: Schematic of beam exit and local dump.

and beam tuning. A 10 inch diameter beam pipe will accommodate all planned scenarios. The beam dump (see Fig. 15) will be constructed above the beam line by stacking concrete blocks movable with the crane.

Similarly configured local dumps were utilized for the Hall C RSS and Gen experiments, and will be used again in 2008 for the SANE group of polarized target experiments. Recently, a Helium bag was also tested in Hall A for the E04-007 experiment which is scheduled to run in March 2008. It successfully withstood approximately 10 times the radiation expected to be produced during E07-001.

5.6 Beamline Instrumentation

5.6.1 Beam Current and Beam Charge Monitor

Beam currents less than 100 nA are typically used with the polarized target in order to limit depolarizing effects and large variations in the density. Standard BCM cavities have a linearity good to 0.2% for currents ranging from 180 down to 1 uA. High accuracy at even lower currents will be possible due to ongoing upgrades, which will be complete before this experiment might be scheduled. Most notably, the Happex III [73] and Lead Parity experiments will require accurate knowledge of the charge and beam position down to 50 nA. We plan to use the low current cavity monitor BCM/BPM sets that were initially tested in 2005. In addition, experiment

E05-004[71] has just recently commissioned a tungsten beam calorimeter, in order to have a good calibration for $I < 3\mu A$. Preliminary results show an absolute calibration of the Hall A BCM with 1% accuracy for currents ranging from 3 μA down to $0.5\mu A$. The calorimeter will be located just after the first BPM and before the first dipole (see Fig. 14). In the worst-case scenario, the tungsten calorimeter will allow at least 2% accuracy [72] on the charge determination all the way down to 50 nA.

5.6.2 Beam Polarimetry

We will utilize the Moeller polarimeter as part of the standard Hall A equipment. During operation, 0.3 to 0.5 μA of current are incident on a foil of iron polarized by a magnetic field. The expected systematic uncertainty [76] of the Moeller measurement is 3.5% or better. An upgrade is planned for the Lead Parity experiment with the goal of reaching 1% systematic. Moeller runs will be scheduled at least once per energy change, and will will be performed with the (non-chicaned) beam passing to the standard hall A dump.

The Compton polarimeter normally is used for a continuous non-invasive beam polarization monitor. However, it is not very well suited to run at low energy or low current. To provide a cross check of the Moller polarimeter, we may dedicate some high current beam time (without polarized target) specifically for Compton polarimeter measurements.

5.7 The Spectrometers

5.7.1 Septa Magnet

The Hall A spectrometers will be fitted with septa magnets allowing to reach scattering angles of 6 and 9 degrees. They have been used successfully for the Hypernuclear experiment, Happex and small angle GDH, so their optical properties are well understood.

5.7.2 Detector Stack

The standard detector stack will be used for detecting electrons. We will require the usual VDC, scintillators S1 and S2, the gas Cerenkov and pion rejector/shower counter for particle identification. Performance of the spectrometers are well known so we can expect the same accuracies as for the GDH experiments on the polarized He3 target E94-010 and E97-110. We note that pion contamination at these kinematics is negligible, as indicated from the epc [88] simulation code.

5.7.3 Optics

A study of the change of the optics coming from the target field was done by John Lerose for the lowest anticipated electron momentum (400 MeV/c). Fig. 16 shows the scattered electrons without field. Fig. 17 displays the effect of the 5 Tesla field. Fig. 18 shows the incident beam corrected by the chicane so that it is horizontal at the target. Except for an approximate 5 mm vertical offset, (which would give about 10^{-3} offset in detected momentum), the shifted envelope looks very much like the no-field situation when it gets to the entrance of the septum. The effect would diminish linearly with either an increase in momentum, or a decrease in the magnetic field. The situation, from an optics point of view, appears to be manageable even in this worst case scenario.

For further detail, Figs. 19 to 22 demonstrate the effect of the 5 T target field on the reconstruction [64]. These plots represent a montecarlo simulation of the target variables δ, θ, ϕ, and y_t. Overall, as the scattered electron momentum decreases, there is a slight degradation in resolution. Shifts in θ (vertical) are also seen along with much smaller shifts in δ and ϕ. The offsets do not have a significant effect since the variables remain in the well known region of the acceptance. The degradation of resolution should result in no worse than a factor of two [64] increase in the systematic uncertainty of the acceptance.

5.7.4 Data Acquisition

We will utilize the standard Hall A data acquisition (DAQ) system which is based on Fastbus 1877 TDC and Fastbus 1881 ADC. The DAQ will be run in two single arm mode which allows up to 4 KHz rate of data for each arm. We will be DAQ rate limited for the lowest few energies.
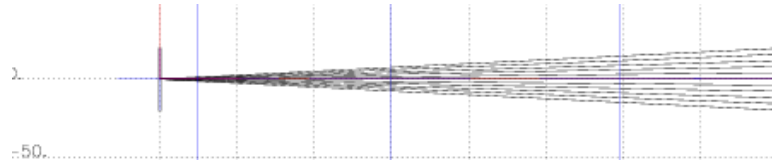
Figure 16: The vertical envelope of 400 MeV/c electron trajectories that would normally go through the spectrometer and septum setup (+-50 mrad).
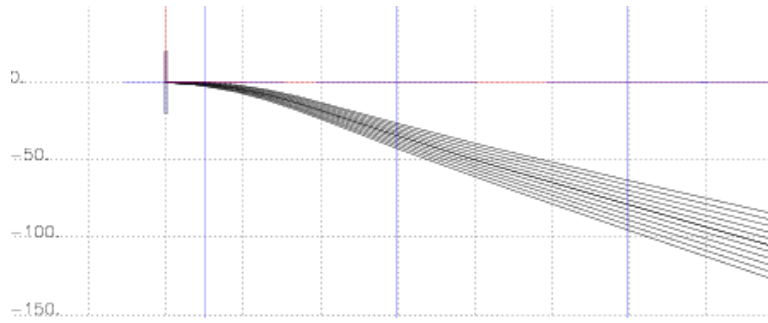
Figure 17: The same envelope of 400 MeV/c trajectories but with the 5 Tesla target field turned on.
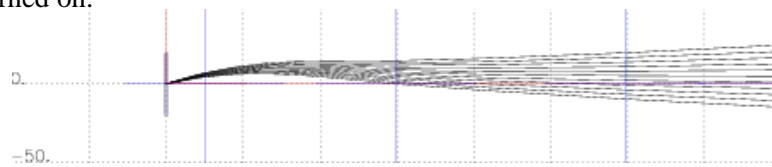
Figure 18: 5 Tesla field remains on but the set of trajectories is vertically shifted by 275 mrad.

37
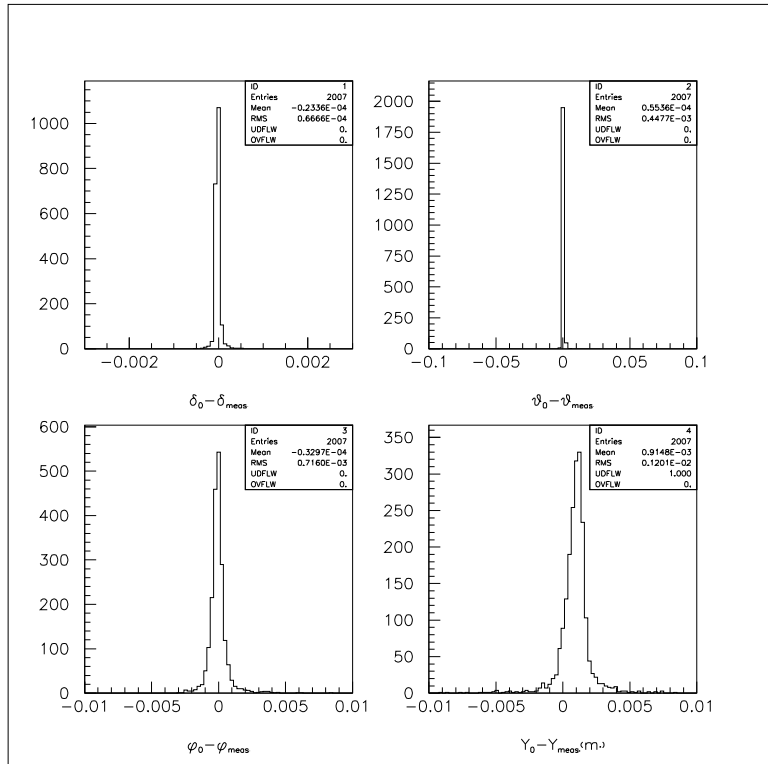
Figure 19: Reconstructed variables : Momentum = 4 GeV/c. Target field = 0 T.
Top left: momentum spread. **Top right:** vertical scattering angle. **Bottom left:** horizontal scattering angle. **Bottom right:** Y-target.
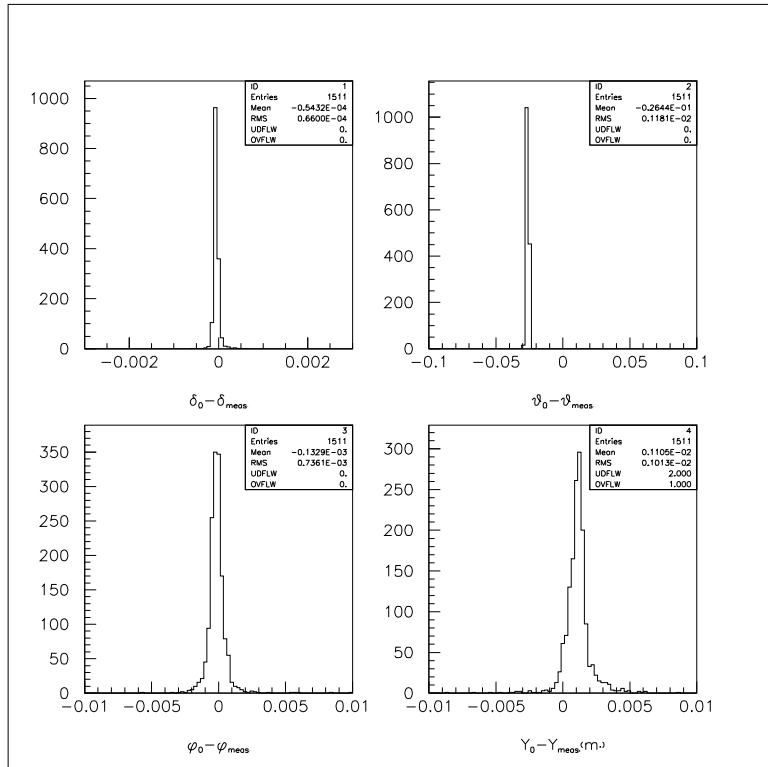
Figure 20: Reconstructed variables : Momentum = 4 GeV/c. Target field = 5 T. **Top left:** momentum spread. **Top right:** vertical scattering angle. **Bottom left:** horizontal scattering angle. **Bottom right:** Y-target.
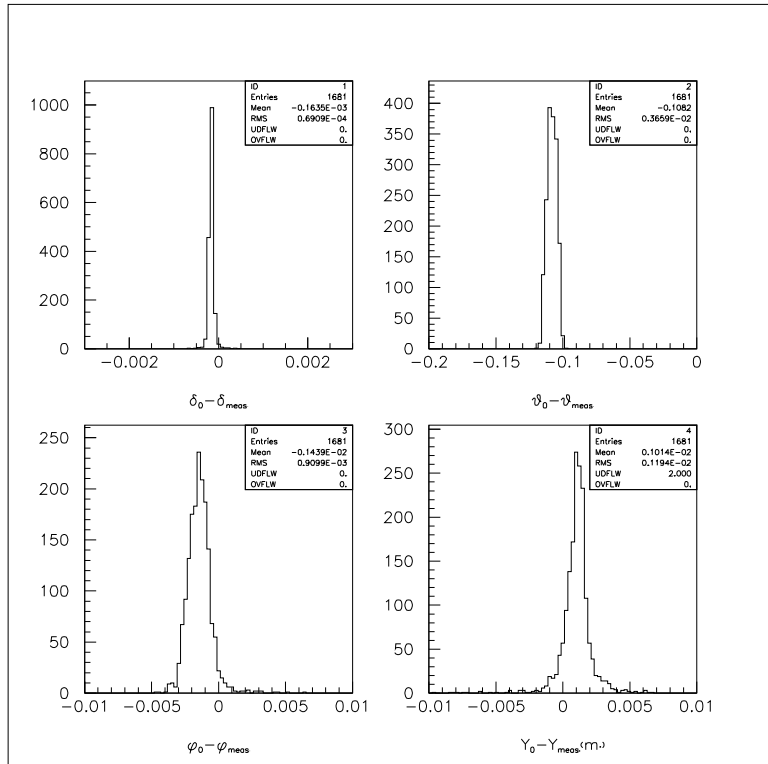
Figure 21: Reconstructed variables : Momentum = 1 GeV/c. Target field = 5 T. **Top left:** momentum spread. **Top right:** vertical scattering angle. **Bottom left:** horizontal scattering angle. **Bottom right:** Y-target.
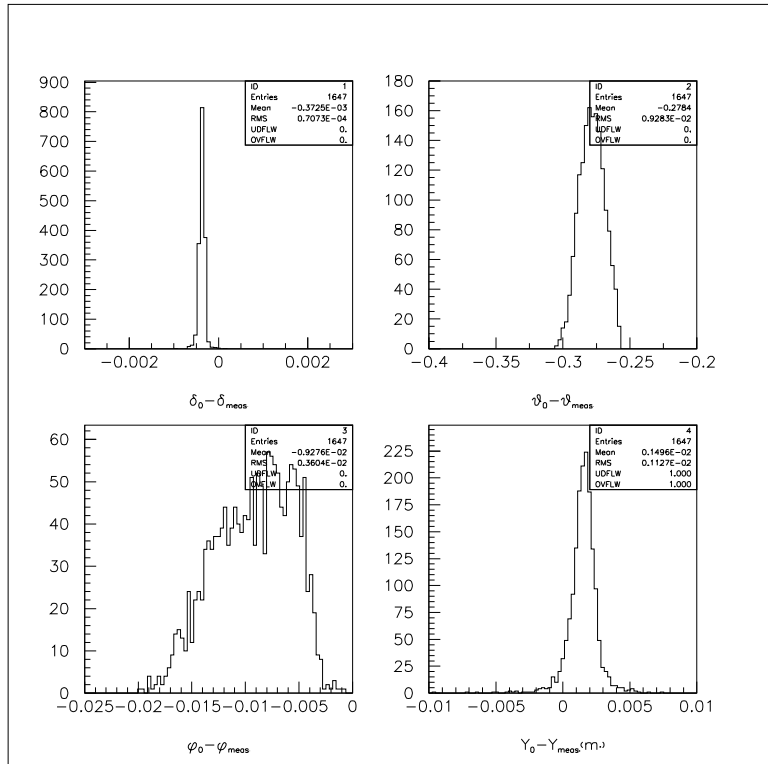
Figure 22: Reconstructed variables : Momentum = 0.4 GeV/c. Target field = 5 T.
Top left: momentum spread. **Top right:** vertical scattering angle. **Bottom left:** horizontal scattering angle. **Bottom right:** Y-target.

6 Analysis Method

6.1 Extraction of the g_2 Structure Function

We will perform a polarized cross section measurement in order to determine the spin structure function g_2^p. The spin structure functions are related to the spin-dependent cross sections via:

$$
\begin{aligned}
g_1 &= \frac{MQ^2}{4\alpha_e^2} \frac{y}{(1-y)(2-y)} \left[\Delta\sigma_\parallel + \tan\frac{\theta}{2}\Delta\sigma_\perp \right] \\
g_2 &= \frac{MQ^2}{4\alpha_e^2} \frac{y^2}{2(1-y)(2-y)} \left[-\Delta\sigma_\parallel + \frac{1+(1-y)\cos\theta}{(1-y)\sin\theta}\Delta\sigma_\perp \right] \quad (26)
\end{aligned}
$$

where $y = \nu/E$.

Here, the polarized cross section differences are represented by $\Delta\sigma_\parallel$ and $\Delta\sigma_\perp$. Measuring polarized cross section differences results in the cancellation of the contribution from any unpolarized target material and obviates the need for any external model input.

We can recast Eq. 26 in the form:

$$
\begin{aligned}
g_1 &= K_1(a_1\Delta\sigma_\parallel + b_1\Delta\sigma_\perp) \\
g_2 &= K_2(c_1\Delta\sigma_\parallel + d_1\Delta\sigma_\perp) \quad (27)
\end{aligned}
$$

where

$$
\begin{aligned}
K_1 &= \frac{MQ^2}{4\alpha_e^2} \frac{y}{(1-y)(2-y)} \\
K_2 &= \frac{MQ^2}{4\alpha_e^2} \frac{y^2}{2(1-y)(2-y)} = K_1\frac{y}{2} \\
a_1 &= 1 \\
b_1 &= \tan\frac{\theta}{2} \\
c_1 &= -1 \\
d_1 &= \frac{1+(1-y)\cos\theta}{(1-y)\sin\theta}
\end{aligned}
$$

Equation 27 reveals that the parallel contribution to g_2 is highly suppressed (See Fig. 23). In fact, the relative weight of the $\Delta\sigma_\parallel$ contribution to g_2 ranges from 2 to 8% for all proposed kinematics. For the kinematics where we will not measure $\Delta\sigma_\parallel$, we will use the high precision data from Hall B experiment EG4 [11], which
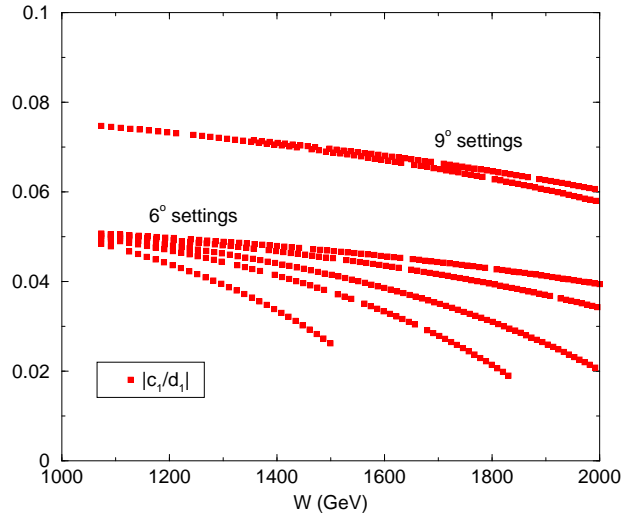
Figure 23: Relative weighting of the $\Delta\sigma_\parallel$ contribution to g_2. See Eq. 27.
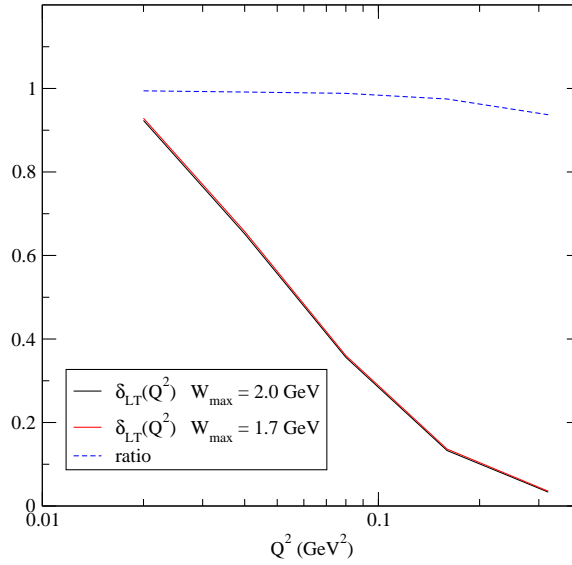
Figure 24: MAID model prediction for $\delta_{LT}(Q^2)$ evaluated with a maximum W of 1.7 and 2.0 GeV, along with the ratio. Over 90% of the integral strength comes from W less than 1.7 GeV.

expects an uncertainty of approximately 10%. Given the ratio of $|c_1/d_1|$, this leads to less than 1% error contribution to our g_2 for all kinematics.

In practice, the EG4 cross section data is not at the exact same kinematics as our proposal, which makes it difficult to directly combine the respective cross sections. Instead, we will use the EG4 g_1 data. Inverting Eq. 26 yields:

$$\Delta\sigma_\parallel = \frac{4\alpha_e^2}{MQ^2}\frac{(1-y)(2-y)}{y}\left(\frac{2}{y}\right)\frac{\frac{1+(1-y)\cos\theta}{(1-y)\sin\theta}\frac{y}{2}\,g_1 - \tan\theta/2\,g_2}{\frac{1+(1-y)\cos\theta}{(1-y)\sin\theta} + \tan\theta/2}$$

$$\Delta\sigma_\perp = \frac{4\alpha_e^2}{MQ^2}\frac{(1-y)(2-y)}{y}\left(\frac{2}{y}\right)\frac{\frac{2}{y}g_1 + g_2}{\frac{1+(1-y)\cos\theta}{(1-y)\sin\theta} + \tan\theta/2} \tag{28}$$

Eq. 28 can be recast in the form:

$$\Delta\sigma_\parallel = K_3(a_2 g_1 + b_2 g_2) \tag{29}$$

$$\Delta\sigma_\perp = K_4(c_2 g_1 + d_2 g_2) \tag{30}$$

where

$$K_3 = \frac{4\alpha_e^2}{MQ^2}\frac{(1-y)(2-y)}{y}\left(\frac{2}{y}\right)\frac{1}{a_2 - b_2}$$

$$K_4 = \frac{4\alpha_e^2}{MQ^2}\frac{(1-y)(2-y)}{y}\left(\frac{2}{y}\right)\frac{1}{a_2 - b_2}$$

$$a_2 = \frac{1+(1-y)\cos\theta}{(1-y)\sin\theta}\frac{y}{2}$$

$$b_2 = -\tan\theta/2$$

$$c_2 = \frac{2}{y}$$

$$d_2 = 1$$

So in terms of the existing Hall B g_1 and the measured $\Delta\sigma_\perp$, g_2 can be expressed:

$$g_2 = \left(\frac{1}{1 - K_2 K_3 c_1 b_2}\right)[d_1\Delta\sigma_\perp + K_2 K_3 c_1 a_2\,g_1] \tag{31}$$

6.2 The Generalized Spin Polarizability δ_{LT}

The generalized Longitudinal-Transverse spin polarizability is given in terms of g_1 and g_2 as:

$$\delta_{LT}(Q^2) = \frac{16\alpha M^2}{Q^6} \int_0^{x_0} x^2 \Big[g_1(x, Q^2) + g_2(x, Q^2) \Big] dx. \tag{32}$$

For the kinematics where we do not measure g_1 directly we will utilize the results of EG4 [11]. Our proposal includes settings (see Table 6) where we will rotate the target and measure $\Delta\sigma_\parallel$ in addition to $\Delta\sigma_\perp$ in order to cross check the Hall B data. Table 9 details the projected EG4 statistical uncertainties [70]. Our beam time request typically aims to match or improve on these errors so that the combined data set is consistent. As for systematic uncertainties, EG4 projects about 10% error, which includes a contribution from their lack of knowledge of transverse data. The effect of our transverse data on the EG4 systematic is discussed in Section 4.2.

6.3 Interpolation to Constant Q^2

The data measured at constant incident energy and scattering angle will be interpolated[†] to constant Q^2 as shown in Fig. 13. The good kinematic coverage and overlap should facilitate a straight forward interpolation.

6.4 Systematic Uncertainties

Several JLab experiments have performed measurements similar to what we propose here (for example, see Refs. [3, 4, 10, 11]). From these previous endeavors, we can make an estimate of the systematic uncertainty. Table 4 gives an estimate of the most significant sources of error, while Table 5 gives further detail on the contributions to the cross section uncertainty which will be the dominant error. Previous experience in Hall A [3] has shown that we can obtain 4-5% systematic uncertainty [66–68] on cross section measurements, with the largest uncertainty (2-3%) coming from the knowledge of the acceptance. Discussion with the Hall A septum/optics expert [64], indicates that, in the worst case, the presence of the 5 Tesla target field and the use of the septum will only increase the acceptance uncertainty by a factor of 2.

An 8%[‡] systematic uncertainty on the moments is assumed in Figs. 25 to 28 of section 7.2. Eq. 32 reveals that the unmeasured low-x contribution to δ_{LT} is suppressed as x^2. In fact, over 90% of the total integral strength (as predicted from the MAID model) is covered in the range from pion threshold to $W = 1.7$ GeV for each of our incident energies. The unmeasured contribution above $W = 2$ GeV is very small and introduces a negligible uncertainty (See Fig. 24).

[†] as has been done in experiments E94010, E97110 and E01012.

[‡] relative to the MAID model prediction.

Source	(%)
Cross section	5-7
Target Polarization	3.0
Beam Polarization	3.0
Radiative Corrections	3.0
Parallel Contribution	≤ 1
^{15}N asymmetry [69]	≤ 1
Total	7-9

Table 4: Total Systematic Uncertainties.

Source	(%)
Acceptance	4-6
Packing fraction	3.0
Charge determination	1.0
VDC efficiency	1.0
PID detector efficiencies	≤ 1
Software cut efficiency	≤ 1
Energy	0.5
Deadtime	0.0
Total	5-7

Table 5: Major contributions to the cross section systematic of Table 4.

7 Rates and Beam Time Request

The count rate of scattered electrons from the polarized target is given by:

$$\dot{N} = \frac{\mathcal{L}\Delta\Omega\Delta E'\sigma}{f} \tag{33}$$

where $\mathcal{L}$ is the luminosity, $\Delta\Omega$ is the angular acceptance, $\Delta E'$ is the momentum bite, σ represents the proton cross section, and f is the dilution factor which accounts for scattering from unpolarized nucleons in the target.

We estimate the experimental cross section by combining proton, nitrogen and helium cross sections from the quasifree scattering model QFS [59, 88]. Inelastic and elastic radiative effects are also included. Table 10 shows the assumed material thickness for a 3 cm target. At the lowest planned Q^2, the elastic radiative tail becomes large and we switch to a thinner (0.5 cm) target cell. Cross-checks with the longer standard cell will help to reduce the systematic uncertainty of the radiative corrections, and ensure we have a good understanding of our target packing fraction. A representative spin-independent cross section is shown in Fig. 29.

The time needed for a given uncertainty δA is given by:

$$T = \frac{1}{\dot{N}(fP_bP_T\delta A)^2} \tag{34}$$

The relevent statistical uncertainty is for the asymmetry, even though this is a cross section measurement, because in the product σA the dominant error arises from A.

The running time and spectrometer configurations are summarized in Table 6. The sixth column represents the rate (in each bin) from the proton, while the seventh shows the total prescaled rate seen by the spectrometer. When the momentum of the scattered electron is accessible by both spectrometers, we double our DAQ rate. We assume a maximum accessible momentum of 3.1 and 4.3 GeV for the right and left HRS respectively. We also assume both spectrometers can reach 0.4 GeV minimum momentum, and that the DAQ limit is 4 kHz per arm[§].

Transverse data will be measured for every kinematic. Table 6 specifies the settings where we plan to also take data with the target polarization held parallel to the beam momentum. This is in order to directly extract g_1 and provide a cross check with the EG4 data. This effectively doubles the time needed for this setting, so the kinematic to perform the longitudinal measurement has been chosen to be at the largest Q^2 for which both arms can simultaneously take data for all chosen momentum settings.

[§]More than 5 kHz rate with manageable deadtime was demonstrated with the existing DAQ during E97110 [10].

To reach the highest Q^2 will require the septum to run 391 A at 6 degrees (P_0=4.15 GeV) and almost 530 A at 9 degrees (P_0=4.0 GeV). Discussion with Hall A septum experts [64, 65] indicate that all of the planned 6 degree settings should be achievable, although the septum must be trained to reach a few of the higher currents required. All of the 9 degree settings are also within the nominal limits, but the 9 degree, 4.0 GeV setting in particular may prove difficult. This has minimal impact on the physics goals of this experiment, since it affects only one kinematic setting at the highest Q^2 (see Fig. 13). To adjust to this circumstance we can perform an extrapolation for the small affected region, or simply reduce our highest expected Q^2 by a small amount.

The choice of parameters used in our rate calculation is summarized in Table 10. We assume an angular acceptance of 4 msr and a momentum acceptance of $\pm4\%$, both slightly reduced from the nominal values due to the presence of the septa, and beam and target polarizations of 80 and 75% respectively. We note that higher polarization values are routinely achieved. Finally, we assume that the minimum time that we would reasonably spend at each setting is one half hour, regardless of how high the rate is.

With this beam request, we achieve $\delta A_\perp = 0.004$ for each 20 MeV bin.

7.1 Overhead

The incident beam causes radiation damage in the frozen ammonia, which leads to the creation [60, 61] of atomic hydrogen in the target material. This provides an additional relaxation path for the nuclear spins, and the buildup of these free radicals leads to a gradual decay of the target polarization. The concentration of these unwanted radicals can be reduced significantly by raising the temperature of the target to 80-90K, in a process known as annealing. Given the proposed beam current and raster size, we expect to require an anneal about once every 14 hours of beam time. The anneal itself typically requires 2.5 hours from start to beam back on target. The target stick holds two ammonia batches. Each batch can absorb approximately $17 \cdot 10^{15}$ e-/cm^2, at which point the material must be replaced. We expect to swap out target inserts about once every 5 days of accumulated (100% efficient) beam. To replace the stick and calibrate the NMR instrumentation requires about a shift.

Measuring g_1 will require physically rotating the target can from the perpendicular to parallel configuration, a process which we estimate will take two shifts. One final overhead arising from the target comes from the need for dedicated empty cell and carbon target runs, which are used to determine the granular target packing fraction and dilution factor. These high rate unpolarized runs can be completed in about one half hour, and we plan to perform them for every other momentum

setting.

Pass changes and linac changes are estimated to require 4 and 8 hours respectively. Changing the spectrometer momentum settings requires approximately 15 minutes each on average, while changes to the septa angle typically takes one shift. We will perform one Moller measurement for each beam energy, each of which requires two hours. Finally, we have included an additional 8 hours of overhead to measure the elastic cross section and asymmetry for the lowest two energies, as a cross check of our beam and target polarizations, and to help ensure we fully understand all cross section systematics.

The overhead requirement is summarized in Table 8. We note that previous experience has shown that many overhead tasks can be performed in parallel, or scheduled to coincide with non-delivery of beam. In this sense, our overhead estimate should be conservative.

7.2 Projected Results

Figs. 25 to 27 show the projected accuracy we can obtain with the beam time request of Table 6. The systematic error bands on the axes represent the total from Table 4. The projected uncertainties have been evaluated assuming the central values predicted by the MAID model [17]. The integral $I_B(Q^2)$ in Fig. 28 corresponds to Eq. 8 when the Gilman convention [89] is chosen for the virtual photon flux factor K.

8 Summary

We request 24 days in order to perform a precision measurement of g_2^p at low and moderate Q^2 using a transversely polarized proton (NH$_3$) target, together with the Hall A HRS and septa. This measurement is needed to provide data on the transverse spin structure of the proton and to resolve several outstanding issues. The Q^2-evolution of $d_2^p(Q^2)$, the BC and extended GDH Sum will be obtained, along with the longitudinal-transverse spin polarizability δ_{LT}, a fundamental quantity which characterizes the nucleon's structure. This data will fill the gap in our knowledge of the proton spin structure function g_2^p, and address intriguing discrepancies between data and theory for the BC Sum Rule and the longitudinal-transverse generalized spin polarizability. It will also have significant impact on ongoing calculations of the hyperfine structure of hydrogen, and substantially reduce one of the leading systematic uncertainties of the EG4 experiment.
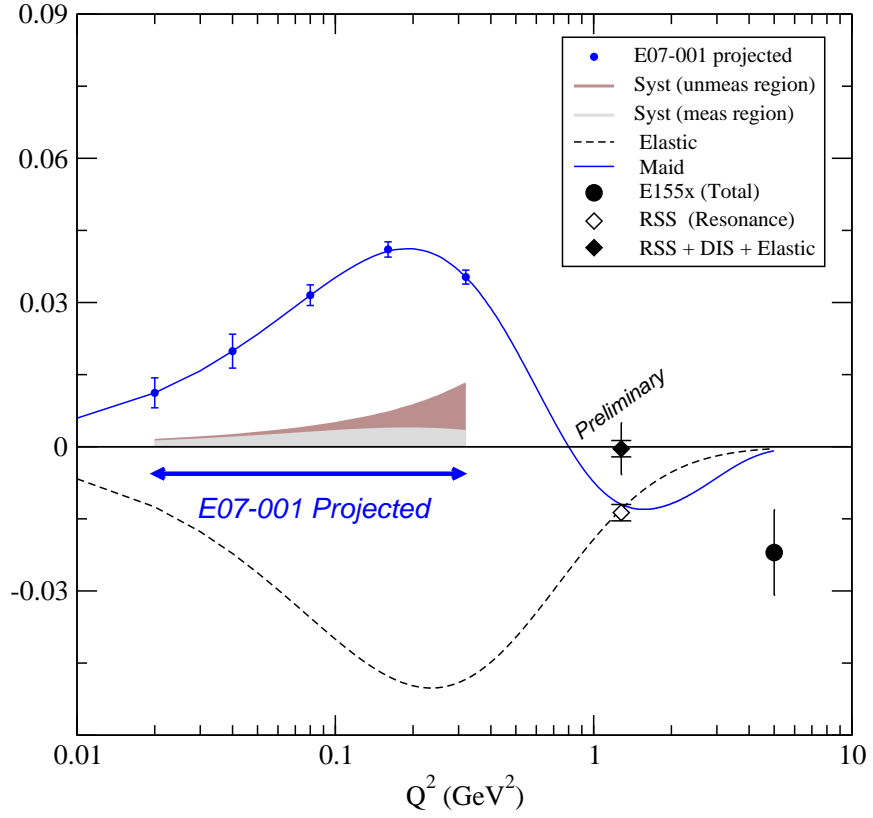
Figure 25: Projected results for Γ_2^p. Statistical errors are shown on the symbols. Systematic for measured region is represented by the light band. Systematic for unmeasured region is represented by the dark band. Uncertainties for the measured region are evaluated assuming the central value predicted by the MAID [17] model. Systematic for the unmeasured region is 100% of the model prediction assuming BC sum rule holds. Elastic curve is from Ref. [62].

50
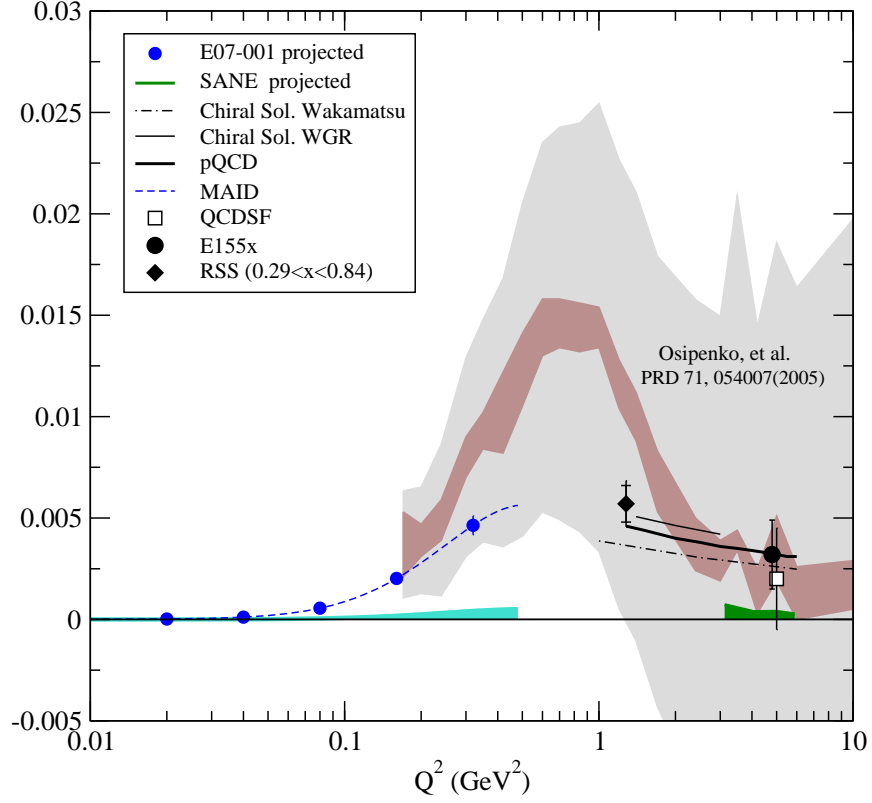
Figure 26: Projected results for d_2^p. Statistical errors are shown on the symbols. Systematic is represented by the band on the axis. Uncertainties are evaluated assuming the central value predicted by the MAID [17] model. Expected SANE uncertainties from Ref [53]. PQCD from Ref. [48]. Lattice QCD calculation from [49]. WGR chiral soliton model from Ref. [32]. Wakamatsu's chiral soliton model from Ref. [33]. Osipenko *et al.* global analysis from Ref. [51]: The inner (outer) band represents statistical (systematic) uncertainty. Unmeasured non-resonance contribution is highly suppressed by x^2 weighting of d_2 and is not shown.

Figure 27: Projected results for δ_{LT}. Statistical errors are shown on the symbols. Systematic is represented by the grey band on the axis. Uncertainties are evaluated assuming the central value predicted by the MAID [17] model. χPT predictions from Bernard *et al.* [38], and Kao *et al.* [39].

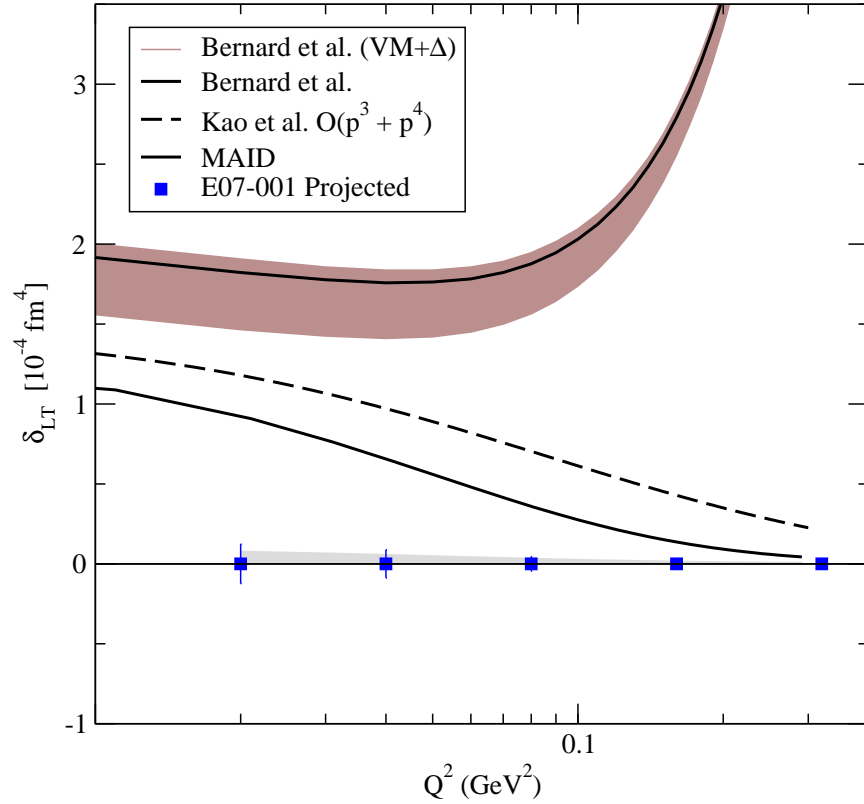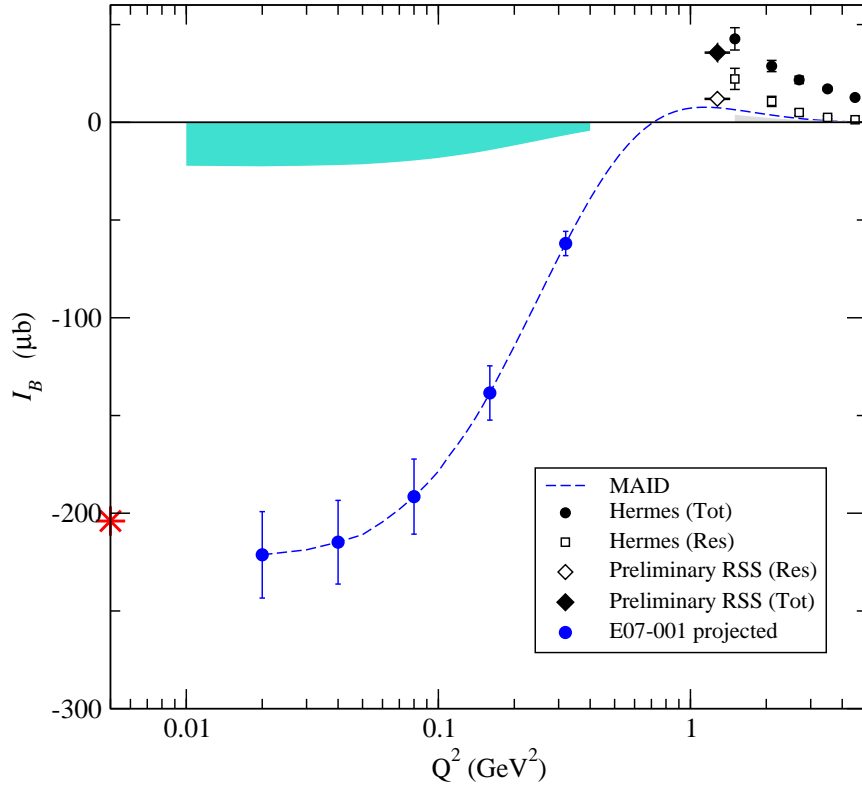Figure 28: Projected results for the GDH Integral $I_{TT}(Q^2)$. Statistical errors are shown on the symbols. Systematic is represented by the band on the axis. Uncertainties are evaluated assuming the central value predicted by the MAID [17] model, scaled here to satisfy the GDH Sum Rule prediction (star). Also shown is HERMES [36], and RSS [4] preliminary data.

A   Beam Time Request Tables

In this section we detail the proposed kinematics and beam time request. In Table 6, all energies and momenta are in GeV, while the luminosity is given in $(cm^2\text{-}s)^{-1}$.

Table 8 summarizes the expected overhead, which was discussed in section 7.1. The expected statistical error is given in Table 9. Table 6 specifies whether we will measure data in the perpendicular configuration alone, or in both perpendicular and parallel configuration for each kinematic. Finally, for reference, in Table 10 we list the relevent experimental parameters that we have assumed in the rate calculation.

Table 6: Beam Time Request.

E_0	Θ	P_0	W	Q^2	Rate P (Hz)	Rate (kHz)	Pre	$\mathcal{L}$	$P_b P_t$	I (nA)	Time (h)
1.1	6	0.950	1.07	0.011	55	4.0	6	0.1E+35	0.60	85	6.7
1.1	6	0.871	1.14	0.010	58	4.0	4	0.1E+35	0.60	85	6.5
1.1	6	0.800	1.20	0.010	70	4.0	3	0.1E+35	0.60	85	5.3
1.1	6	0.734	1.25	0.009	82	4.0	3	0.1E+35	0.60	85	4.5
1.1	6	0.674	1.29	0.008	86	4.0	2	0.1E+35	0.60	85	4.3
1.1	6	0.618	1.33	0.007	93	4.0	2	0.1E+35	0.60	85	4.0
1.1	6	0.567	1.37	0.007	103	4.0	2	0.1E+35	0.60	85	3.6
1.1	6	0.521	1.40	0.006	113	4.0	2	0.1E+35	0.60	85	3.3
1.1	6	0.478	1.43	0.006	125	4.0	2	0.1E+35	0.60	85	3.0
1.1	6	0.439	1.45	0.005	139	4.0	2	0.1E+35	0.60	85	2.7
1.1	6	0.403	1.48	0.005	154	4.0	2	0.1E+35	0.60	85	2.4
1.1	6	0.369	1.50	0.004	170	4.0	2	0.1E+35	0.60	85	2.2
										1.0	days
1.7	6	1.540	1.07	0.029	46	4.0	2	0.1E+35	0.60	85	8.0
1.7	6	1.414	1.18	0.026	54	4.0	2	0.1E+35	0.60	85	6.9
1.7	6	1.297	1.27	0.024	66	4.0	1	0.1E+35	0.60	85	5.6
1.7	6	1.191	1.35	0.022	65	4.0	1	0.1E+35	0.60	85	5.7
1.7	6	1.093	1.41	0.020	72	4.0	1	0.1E+35	0.60	85	5.1
1.7	6	1.003	1.47	0.019	83	4.0	1	0.1E+35	0.60	85	4.5
1.7	6	0.920	1.53	0.017	93	4.0	1	0.1E+35	0.60	85	4.0
1.7	6	0.845	1.57	0.016	96	4.0	1	0.1E+35	0.60	85	3.9
1.7	6	0.775	1.61	0.014	98	3.9	1	0.1E+35	0.60	85	3.8
1.7	6	0.712	1.65	0.013	103	3.8	1	0.1E+35	0.60	85	3.6
1.7	6	0.653	1.68	0.012	113	4.0	1	0.1E+35	0.60	85	3.3
1.7	6	0.599	1.71	0.011	122	4.0	1	0.1E+35	0.60	85	3.1
1.7	6	0.550	1.74	0.010	129	4.0	1	0.1E+35	0.60	85	2.9
1.7	6	0.505	1.76	0.009	138	4.0	1	0.1E+35	0.60	85	2.7
1.7	6	0.463	1.79	0.009	147	4.0	1	0.1E+35	0.60	85	2.5
1.7	6	0.425	1.81	0.008	158	4.0	1	0.1E+35	0.60	85	2.4
1.7	6	0.390	1.83	0.007	170	4.0	1	0.1E+35	0.60	85	2.2
										1.5	days
2.2	6	2.030	1.07	0.049	45	4.0	13	0.8E+35	0.60	85	8.2
2.2	6	1.863	1.21	0.045	54	4.0	11	0.8E+35	0.60	85	6.9
2.2	6	1.709	1.33	0.041	58	4.0	8	0.8E+35	0.60	85	6.4
2.2	6	1.569	1.42	0.038	65	4.0	6	0.8E+35	0.60	85	5.7
2.2	6	1.440	1.51	0.035	77	4.0	5	0.8E+35	0.60	85	4.9
2.2	6	1.321	1.58	0.032	80	4.0	5	0.8E+35	0.60	85	4.7
2.2	6	1.213	1.64	0.029	83	4.0	4	0.8E+35	0.60	85	4.5

Table 6: Beam Time Request.

E_0	Θ	P_0	W	Q^2	Rate P (Hz)	Rate (kHz)	Pre	$\mathcal{L}$	$P_b P_t$	I (nA)	Time (h)
2.2	6	1.113	1.70	0.027	87	4.0	4	0.8E+35	0.60	85	4.3
2.2	6	1.022	1.75	0.025	89	4.0	4	0.8E+35	0.60	85	4.2
2.2	6	0.938	1.80	0.023	93	4.0	4	0.8E+35	0.60	85	4.0
2.2	6	0.860	1.84	0.021	96	4.0	5	0.8E+35	0.60	85	3.9
2.2	6	0.790	1.87	0.019	101	4.0	5	0.8E+35	0.60	85	3.7
2.2	6	0.725	1.91	0.017	107	4.0	5	0.8E+35	0.60	85	3.5
2.2	6	0.665	1.94	0.016	113	4.0	5	0.8E+35	0.60	85	3.3
2.2	6	0.610	1.96	0.015	120	4.0	6	0.8E+35	0.60	85	3.1
2.2	6	0.560	1.99	0.013	128	4.0	6	0.8E+35	0.60	85	2.9
2.2	6	0.514	2.01	0.012	137	4.0	7	0.8E+35	0.60	85	2.7
										1.6	days
3.3‡	6	3.096	1.07	0.112	29	4.0	7	0.8E+35	0.60	85	12.7
3.3‡	6	2.841	1.28	0.103	39	4.0	6	0.8E+35	0.60	85	9.4
3.3‡	6	2.608	1.44	0.094	42	4.0	4	0.8E+35	0.60	85	8.7
3.3‡	6	2.393	1.58	0.087	50	4.0	3	0.8E+35	0.60	85	7.5
3.3‡	6	2.196	1.69	0.079	54	4.0	2	0.8E+35	0.60	85	6.9
3.3‡	6	2.016	1.79	0.073	57	4.0	2	0.8E+35	0.60	85	6.5
3.3‡	6	1.850	1.88	0.067	61	4.0	2	0.8E+35	0.60	85	6.1
3.3‡	6	1.698	1.96	0.061	65	4.0	1	0.8E+35	0.60	85	5.7
3.3‡	6	1.558	2.02	0.056	69	4.0	1	0.8E+35	0.60	85	5.4
										2.9	days
4.4	6	4.149†	1.07	0.200	22	4.0	5	0.8E+35	0.60	85	16.7
4.4	6	3.808†	1.34	0.184	29	4.0	4	0.8E+35	0.60	85	12.9
4.4	6	3.495†	1.55	0.168	33	4.0	2	0.8E+35	0.60	85	11.4
4.4	6	3.207†	1.72	0.155	34	4.0	2	0.8E+35	0.60	85	10.7
4.4	6	2.944	1.86	0.142	36	4.0	1	0.8E+35	0.60	85	10.3
4.4	6	2.701	1.98	0.130	40	4.0	1	0.8E+35	0.60	85	9.4
4.4	6	2.479	2.09	0.120	44	4.0	1	0.8E+35	0.60	85	8.4
										2.7	days
4.4	9	4.023†	1.07	0.436	14	2.5	1	0.8E+35	0.60	85	25.2
4.4	9	3.692†	1.34	0.400	17	2.2	1	0.8E+35	0.60	85	21.4
4.4	9	3.389†	1.55	0.367	16	2.0	1	0.8E+35	0.60	85	22.4
4.4	9	3.110†	1.72	0.337	14	1.7	1	0.8E+35	0.60	85	25.6
4.4	9	2.854	1.86	0.309	12	1.4	1	0.8E+35	0.60	85	31.2
4.4	9	2.620	1.98	0.284	11	1.2	1	0.8E+35	0.60	85	33.1
4.4	9	2.404	2.09	0.260	11	1.1	1	0.8E+35	0.60	85	33.7
										6.0	days

† signifies that only the left spectrometer can access this momentum.
‡ signifies that longitudinal data will be taken in addition to transverse.

Table 7: Beam Request Summary.

Days using 1 (2) arms	25.2	(15.7)
Days for Overhead	8.4	(8.4)
Total Days using 1 (2) arms	33.6	(24.1)

Table 8: Overhead

Overhead	Number	Time Per (hr)	(hr)
Target anneal	27	2.5	67.5
Target rotation	2	16.0	32.0
Target swap	2	8.0	16.0
Pass change	6	4.0	24.0
Packing Fraction	34	0.50	17.0
Linac change	0	8.0	0.0
Momentum change	69	0.25	17.2
Moller measurement	6	2.0	12.0
Septum angle change	1	8.0	8.0
Elastic calibration	2	4.0	8.0
			201.8

Table 9: Statistical Uncertainty

Kinematic	$A_\parallel$ error	$A_\perp$ error
1	0.004*	0.004
2	0.004*	0.004
3	0.004*	0.004
4	0.004	0.004
5	0.004*	0.004
6	0.004*	0.004

* EG4 expected uncertainty.

Table 10: Experiment Parameters

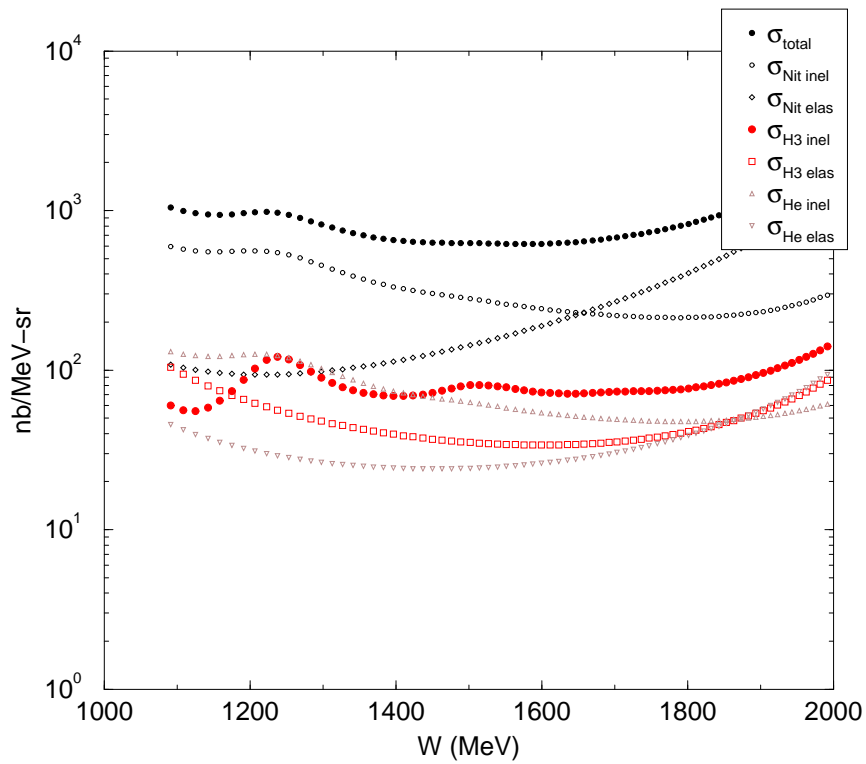| Parameter	Value
$\Delta\Omega$ [msr]	4.0
$\pm\delta P$[%]	4.0
P_{Target} [%]	75.0
P_{Beam} [%]	80.0
T_b radiation length	0.026
T_a radiation length	0.026
Minimum time per setting [hr]	0.5
Minimum Momentum [MeV]	400.0
Maximum Momentum (L) [MeV]	4300.0
Maximum Momentum (R) [MeV]	3100.0
Daq Limit [kHz]	4.0
Packing Fraction	0.55

Figure 29: NH$_3$ cross section at $E_0 = 2.2$ GeV, 6°.

References

[1] See, *e.g.*, B. W. Filippone and X. Ji, Adv. Nucl. Phys. **26**, 1 (2001).

[2] J. D. Bjorken, Phys. Rev. **148**, 1467 (1966).

[3] M. Amarian *et al.*, Phys. Rev. Lett. **89**, 242301 (2002);**92**, 022301 (2004);**93**, 152301 (2004); K. Slifer, *et al.*, [E94010 Collaboration] in preparation.

[4] JLab RSS experiment, M. Jones and O Rondon, spokespersons ; F. R. Wesselmann *et al.* Phys. Rev. Lett. **98**, 132003 (2007). K. Slifer, *et al.*, [RSS Collaboration] in preparation.

[5] R. Fatemi *et al.*, Phys. Rev. Lett. **91**, 222002 (2003).

[6] J. Yun *et al.*, Phys. Rev. **C 67**, 055204 (2003).

[7] A. Deur *et al.*, Phys. Rev. Lett. **93**, 212001 (2004).

[8] K.V. Dharmawardane *et al.*, Phys. Lett. **B 641** 11 (2006); Y. Prok *et al.*, to be published.

[9] J.-P. Chen, A. Deur and Z.-E. Meziani, Mod. Phys. Lett. **A 20**, 2745 (2005); J.-P. Chen, nucl-ex/0611024 (2006).

[10] JLab experiment E97-110, J. P. Chen, A. Deur, F. Garibaldi, spokespersons.

[11] JLab run group Eg4, M. Battaglieri, R. De Vita, A. Deur, M. Ripani spokespersons. http://www.jlab.org/exp_prog/proposals/03/PR03-006.pdf

[12] JLab E01-012, J. P. Chen, S. Choi and N. Liyanage, spokespersons.

[13] J. Callan, G. Curtis. and D. J. Gross, Phys. Rev. Lett. **22**, 156 (1969).

[14] R. L. Jaffe, Comments Nucl. Part. Phys. **19**, 239 (1990).

[15] S. Wandzura and F. Wilczek, Phys. Lett. **B72**, 195 (1977).

[16] S. B. Gerasimov, Sov. J. Nucl. Phys. **2**, 598 (1965); S. D. Drell and A. C. Hearn, Phys. Rev. Lett. **16**, 908 (1966).

[17] D. Drechsel, S. S. Kamalov and L. Tiator, Phys. Rev. **D 63**, 114010 (2001).

[18] X. Ji and J. Osborne, J. of Phys. G **27**, 127 (2001).

[19] D. Drechsel, B. Pasquini and M. Vanderhaeghen, Phys. Rep. **378**, 99 (2003); D. Drechsel and L. Tiator, Ann. Rev. Nucl. Part. Sci. **54**, 69 (2004).

[20] H. Burkhardt and W. N. Cottingham, Ann. Phys. (N.Y.) **56**, 453 (1970).

[21] A. V. Manohar, arXiv:hep-ph/9204208.

[22] R. L. Jaffe and X.-D. Ji, Phys. Rev. **D43**, 724 (1991).

[23] J. Soffer and O. V. Teryaev, Phys. Lett. **B545**, 323 (2002) .

[24] V. Bernard, N. Kaiser, and U.-G. Meissner, Int. J. Mod. Phys. **E4**, 193 (1995).

[25] A. W. Thomas and W. Weise, *The Structure of the Nucleon* (Wiley-Vch, Berlin, 2001).

[26] P. L. Anthony *et al.* [E155 Collaboration], Phys. Lett. B **553**, 18 (2003) [arXiv:hep-ex/0204028].

[27] K. Kramer *et al.*, Phys. Rev. Lett. **95**, 142002 (2005) [arXiv:nucl-ex/0506005].

[28] S. Simula, M. Osipenko, G. Ricco and M. Taiuti, Phys. Rev. D **65**, 034017 (2002) [arXiv:hep-ph/0107036].

[29] J. Yun *et al.*, Phys. Rev. C **67** 055204, (2003); S. Kuhn, private communication.

[30] M. Stratmann, Z. Phys. C **60**, 763 (1993).

[31] X. Song, Phys. Rev. D **54**, 1955 (1996).

[32] H. Weigel and L. Gamberg, Nucl. Phys. A **680**, 48 (2000); Weigel, Gamberg and Reinhardt, Phys. Rev. **D55** (1997) 6910.

[33] M. Wakamatsu, Phys. Lett. B **487**, 118 (2000).

[34] K. Abe *et al.*, Phys. Rev. **D 58**,112003 (1998).

[35] Z. E. Meziani *et al.*, Phys. Lett. B **613**, 148 (2005) [arXiv:hep-ph/0404066].

[36] A. Airapetian *et al.* [HERMES Collaboration], Eur. Phys. J. C **26**, 527 (2003)

[37] K. Ackerstaff *et al.*, Phys. Lett. **B 404**, 383 (1997); **B 444**, 531 (1998).

[38] V. Bernard, T. Hemmert and Ulf-G. Meissner, Phys. Lett.

[39] C. W. Kao, T. Spitzenberg and M. Vanderhaeghen, Phys. Rev. **D 67**, 016001 (2003).

[40] V. Olmos de Leon *et al.*, Eur. Phys. J. **A 10**, 207 (2001); J. Tonnison *et al.*, Phys. Rev. Lett. **80**, 4382 (1998).

[41] J. Ahrens *et al.*, Phys. Rev. Lett. **87**, 022003 (2001).

[42] P. A. M. Guichon, G. Q. Liu and A. W. Thomas, Nucl. Phys. **A 591**, 606 (1995).

[43] P. E. Bosted *et al.* [CLAS Collaboration], Phys. Rev. C **75**, 035203 (2007) [arXiv:hep-ph/0607283].

[44] N. I. Kochelev et al, Phys. Rev. D **67**, 074014 (2003), and private communication.

[45] Marc Vanderhaeghen, JLab Theory Division, private communication.

[46] Christian Weiss, JLab Theory Division, private communication.

[47] X. Zheng *et al.*, Phys. Rev. **C 70**, 065207 (2004).

[48] Edward V. Shuryak and A.I. Vainshtein. Nucl. Phys. **B201** (1982) 141.

[49] M. Gockeler *et al.* Phys. Rev. **D 63**, 074506 (2001). hep-lat/0011091

[50] M. Stratmann, Z. Phys. **C60** (1993) 763.

[51] M. Osipenko *et al.*, Phys. Rev. D **71**, 054007 (2005).

[52] P. L. Anthony *et al.*, Phys. Lett. **B553** (2003) 18.

[53] Hall C Sane experiment. O. Rondon, Z.-E. Meziani and S. Choi spokesmen. Scheduled to run in 2008.

[54] J. Soffer and O. V. Teryaev, Phys. Rev. **D 70**, 116004 (2004).

[55] V. D. Burkert and B. L. Ioffe, Phys. Lett. **B 296**, 223 (1992).

[56] X. Ji, C. Kao, and J. Osborne, Phys. Lett. B **472**, 1 (2000).

[57] JLab experiment E06-014, S. Choi, X. Jiang, Z.E. Meziani and B. Sawatzky spokespersons.

[58] JLab experiment E12-06-121, T. Averett, W. Korsch, Z.E. Meziani and B. Sawatzky, spokespersons.

[59] K. Slifer, E94010 Technical Note #44: "Modifications to the QFS and RAD-COR Codes", (2003).

[60] P. M. McKee NIM A526 (2004) 60-64.

[61] L. De Marco, A, Brill, D. Crabb, J. Chem. Phys. 108 (1998) 1423.

[62] E. L. Lomon , PRC 66 04501 (2002).

[63] M. Amarian *et al.* [Jefferson Lab E94-010 Collaboration], Phys. Rev. Lett. **92**, 022301 (2004) [arXiv:hep-ex/0310003].

[64] J. Lerose, Hall A Staff. Private communication.

[65] R. Feuerbach, Hall A Staff. Private communication.

[66] K. Slifer, E94010 Technical Note #37 : "Dependence of the Cross-Section on Acceptance Cuts for E94010", (2001)

[67] K. Slifer, E94010 Technical Note #38 : "E94010 Unpolarized ^{3}He Cross Sections", (2001)

[68] K. Slifer, Ph.D. Thesis. Temple University (2004).

[69] Mark Jones, "*The ^{15}N correction to the measured asymmetries*", RSS technical note 2005-01 (2005).

[70] M. Ripani's EG4 analysis webpage :
http://www.jlab.org/Hall-B/secure/eg4/ripani/analysis.html

[71] JLab E05-004 : R. Gilman, D.W. Higinbotham, X. Jiang, spokespersons.
'$A(Q)$ at low Q in eD Elastic Scattering'.

[72] Private communication, Arne Freyberger.

[73] L. Kaufman, K. Pascke, R. Michaels, "Cavity Monitor Performance in
2005", http://hallaweb.jlab.org/experiment/HAPPEX/docs/, HAPPEX tech-
note, (2006).

[74] J. Benesch, JLab Center for Advanced Studies of Accelerators (CASA). pri-
vate communication.

[75] C. Yan, R. Carlini, "Chicane and raster system for Hall C", CEBAF-R-92-
004, (1992).

[76] J. Alcorn *et al.*, Nucl. Instrum. Meth. A **522**, 294 (2004).

[77] V. Nazaryan, C. E. Carlson and K. A. Griffioen, Phys. Rev. Lett. **96**, 163001
(2006) [arXiv:hep-ph/0512108].

[78] PR-07-004 : J. Arrington, D. Day, R. Gilman, G. Ron(contact). Update sub-
mitted to PAC33.

[79] A. C. Zemach, Phys. Rev. **104**, 1771 (1956).

[80] C. K. Iddings, Phys. Rev. **138**, B446 (19 65).

[81] R. N. Faustov and A. P. Martynenko, Eur. Phys. J. C **24**, 281 (2002);
R. N. Faustov and A. P. Martynenko, Phys. Atom. Nucl. **65**, 265 (2002) [Yad.
Fiz. **65**, 291 (2002)].

[82] E. De Rafael, Phys. Lett. B **37**, 201 (1971).

[83] P. Gnädig and J. Kuti, Phys. Lett. B **42**, 241 (1972).

[84] S. D. Drell and J. D. Sullivan, Phys. Rev. **154**, 1477 (1967).

[85] A. V. Volotka, V. M. Shabaev, G. Plunien and G. Soff, Eur. Phys. J. D **33**, 23
(2005).

[86] Mainz Proposal A1/01-00: "Double polarization Virtual Compton Scattering
in the threshold regime". http://wwwa1.kph.uni-mainz.de/A1/publications/
proposals/

[87] H. Fonvieille, "Virtual Compton scattering at low energy and the general-
ized polarizabilities of the nucleon," Prog. Part. Nucl. Phys. **55**, 198 (2005)
[arXiv:hep-ph/0412074].

[88] J.W. Lightbody Jr. and J.S. O'Connell, Computers in Physics,57 May/June
1988.

[89] F. J. Gilman, Phys. Rev. **167**, 1365 (1968).